



Coupled estimation of 500 m and 8-day resolution global evapotranspiration and gross primary production in 2002–2017

Yongqiang Zhang^{a,b,*}, Dongdong Kong^{a,c,*}, Rong Gan^{a,d}, Francis H.S. Chiew^a, Tim R. McVicar^a, Qiang Zhang^e, Yuting Yang^f

^a CSIRO Land and Water, GPO Box 1700, Acton 2601, Canberra, Australia

^b Institute of Geographic Sciences and Natural Resources Research, Chinese Academy of Sciences, Beijing 100101, China

^c Department of Water Resources and Environment, Sun Yan-Sen University, Guangzhou 510275, China

^d School of Life Sciences, University of Technology Sydney, NSW 2007, Australia

^e Key Laboratory of Environmental Changes and Natural Hazards, Ministry of Education, Academy of Hazard Reduction and Emergency Management & State Key Laboratory of Earth Surface Processes and Resource Ecology, Beijing, China

^f State Key Laboratory of Hydrosience and Engineering, Department of Hydraulic Engineering, Tsinghua University, Beijing 100084, China

ARTICLE INFO

Keywords:

Global
Terrestrial
Evapotranspiration
Gross primary production
Stomatal conductance
MODIS
Leaf area index

ABSTRACT

Accurate quantification of terrestrial evapotranspiration (ET) is essential to understand the Earth's energy and water budgets under climate change. However, despite water and carbon cycle coupling, there are few diagnostic global evapotranspiration models that have complete carbon constraint on water flux run at a high spatial resolution. Here we estimate 8-day global ET and gross primary production (GPP) at 500 m resolution from July 2002 to December 2017 using a coupled diagnostic biophysical model (called PML-V2) that, built using Google Earth Engine, takes MODIS data (leaf area index, albedo, and emissivity) together with GLDAS meteorological forcing data as model inputs. PML-V2 is well calibrated against 8-day measurements at 95 widely-distributed flux towers for 10 plant functional types, indicated by Root Mean Square Error (RMSE) and Bias being 0.69 mm d^{-1} and -1.8% for ET respectively, and being $1.99 \text{ g C m}^{-2} \text{ d}^{-1}$ and 4.2% for GPP. Compared to that performance, the cross-validation results are slightly degraded, with RMSE and Bias being 0.73 mm d^{-1} and -3% for ET, and $2.13 \text{ g C m}^{-2} \text{ d}^{-1}$ and 3.3% for GPP, which indicates robust model performance. The PML-V2 products are noticeably better than most GPP and ET products that have a similar spatial resolution, and suitable for assessing the influence of carbon-induced impacts on ET. Our estimates show that global ET and GPP both significantly ($p < 0.05$) increased over the past 15 years. Our results demonstrate it is very promising to use the coupled PML-V2 model to improve estimates of GPP, ET and water use efficiency, and its uncertainty can be further reduced by improving model inputs, model structure and parameterisation schemes.

1. Introduction

Terrestrial evapotranspiration (ET) is the sum of evaporation from the soil, E_s , transpiration from the plant canopy, E_t , and evaporation of precipitation intercepted by the vegetation, E_i :

$$ET = E_s + E_t + E_i \quad (1)$$

Among the three components, E_t is coupled with carbon assimilation (or gross primary productivity (GPP)), forming the two dominant processes in global water and carbon cycles (Cowan, 1982; Jasechko et al., 2013; Jung et al., 2010; Keenan et al., 2013; Maxwell and Condon, 2016; Monteith, 1964). The other components E_s and E_i may be indirectly linked with GPP as E_s decreases and E_i increases associated with

GPP increases, especially when the vegetation cover increases (Zhang et al., 2016). Better understanding of these interrelated processes will improve our ability to manage water and carbon resources. ET forms the second largest water flux within the terrestrial hydrological cycle, accounting for about 60–70% of precipitation globally (Oki and Kanae, 2006; Trenberth et al., 2007; Zhang et al., 2016). GPP is produced during photosynthesis and provides a key source of food and energy to sustain the vast majority of life on Earth. Therefore, it is critical to accurately estimate global ET and GPP under climate change and land-cover change.

Numerous global ET and/or GPP studies have been conducted over the past 10 years (Table 1). There are two key findings from this survey of previous studies. First, there are only few moderate resolution (\leq

* Corresponding authors at: Address: CSIRO Land and Water, Clunies Ross Street, Canberra 2601, Australia.

E-mail addresses: yongqiang.zhang2014@gmail.com (Y. Zhang), kongdd.sysu@gmail.com (D. Kong).

Table 1
Summary of major global ET and GPP products. In the 'Model Scheme' column ML means Machine Learning, PM-RS refers to Penman-Monteith models that are forced with Remote Sensing, PT means Priestley-Taylor, WB denoted Water Balance, RG regression, LSM is a Land Surface Model, and LUE refers to Light Use Efficiency.

Dataset Variable	Model Scheme	Product Name	Temporal cover	Temporal Resolution	Spatial Resolution	Algorithm	Validation	Note	Reference(s)
ET	ML	MTE	1982–2011	monthly	0.5°	Model Tree Ensemble (MTE)	253 EC sites (global)	Machine learning used	Jung et al. (2009) and Jung et al. (2010b)
	PM-RS	MOD16A2/A3	2001Jan-present	8-day, annual	500 m	Penman-Monteith-RS	72 EC sites (AmeriFlux)	Used for MOD16 products	Mu et al. (2007) and Mu et al. (2011)
	PM-RS	PML	1998–2012	monthly	0.5°	PML-RS, WB	95 EC sites, 643 catchment streamflow (global)	Components of Et, Es, Ei separated	Zhang et al. (2016)
	PM-RS	LST	2000–2013	daily	0.05°, 0.25°	Penman-Monteith-RS	39 EC sites (AmeriFlux)	Obtained using four conditions: wet/dry and vegetated/non-vegetated	Raoufi and Beighley (2017)
	PM-RS	PM-Gs	2001–2011	daily	1 km	Reverse PM Gs	16 EC sites (global)	Surface conductance is reversed calculated from PM equation	Yebra et al. (2015)
	PT	Priestley-Taylor	1986–1993	monthly	1°	Priestley-Taylor PET to ET	16 EC sites (global)	Components of Et, Es, Ei separated	Fisher et al. (2008)
	PT	GLEAM	1980–2016	daily	0.25°	Priestley-Taylor equation	43 EC sites, 24 catchment streamflow (global)	Components of Ei, Et, Es, sublimation separated	Miralles et al. (2011a) and Miralles et al. (2011b)
	WB	WB	1982–2009	annual	0.5°	Water balance equation	59 major catchment streamflow (global)	GRACE to account change in water storage	Zeng et al. (2012)
	RG	Regression	1986–1995	monthly	1°	Regression equation	12 EC sites (AmeriFlux), 8 enhanced surface facility (EF) sites (America)	Using vegetation index and daily average temperature for regression	Wang and Liang (2008)
	LSM	CLM ET	1982–2010	monthly	1°	CLM simulation	Not performed	Three products: GLEAM, MTE, and CLM4.5	Dong and Dai (2017)
GPP	LSM	GSWP-2	1986–1995	daily	1°	GSWP LSM simulations	3 EC sites (AmeriFlux)	The difference between models is large	Schlosser and Gao (2010)
	ML	MTE GPP	1980–2013	daily	0.5°	Model Tree Ensemble (MTE)	224 EC sites	ML methods: Random Forests, Artificial Neural Networks, Multivariate Adaptive Regression Splines	Jung et al. (2017) and Tramontana et al. (2016)
	LUE	MOD17A2	2000Feb-present	8-day	500 m, 1 km	LUE	Not performed	Used for MOD17 products	Running et al. (2015)
	LSM	BEPS GPP	2000–2015	hourly, daily, monthly, annual	36 km	BEPS model	Not performed	Soil moisture data from SWAP assimilated in BEPS	He et al. (2017)
	LUE	VPM GPP V20	2000–2016	8-day, monthly, annual	500 m, 0.05°, 0.5°	LUE (VPM)	113 EC sites (global)	VI gap-filling and smoothing algorithm, separate treatment for C3/C4 photosynthesis pathways	Zhang et al. (2017a)
	LSM	JULES-WFDEI-GPCC	2001–2010	monthly	0.5°, 1°, 2°	JULES, process based model	MODIS, FLUXNET-MTE, CARDAMOM GPP	Multiple meteorological datasets used (WFDEI-GPCC, WFDEI-CRU and PRINCETON)	Slevin et al. (2017)
	LSM	TRENDY v3 ensemble	1980–2013	daily	0.5°	dynamic global vegetation model	Not performed	LSM models used: CABLE, ISAM, LPJ, LPJ-GUESS, ORCHIDEE, VEGAS, VISIT	Jung et al. (2017)
	LSM	Ensemble GPP of 8 ISIMP terrestrial biome models	1971–2010	(half) hourly to monthly	0.5°	process based or LUE	Not performed	eight ISIMP2a biome models: CARAIB, DLEM, JULES, LPJm1, LPJ-GUESS, ORCHIDEE, VEGAS, and VISIT	Chen et al. (2017)
	MTE, LUE, ML, LSM	Ensemble GPP of 11 models	1998–2005	daily, monthly, annual, long-term	1 km, 0.5°, watershed	MTE, LUE, WUE, Look-up-table, diagnostic or process based GDVM	253 EC sites (global)	Models used: MTE, MIAMI, ANN, LUE, WUE, KGB, LPJ-DGVM, LPJm1, ORCHIDEE, CLM-CN, SDGVM	Beer et al. (2010)
	LSM	ET of 15 models	1959–2016	6-hourly, monthly	0.3°–5°	Carbon observation from ocean and land	Carbon observation from ocean and land	Models used: CABLE, CLASS-CTEM, CLM4.5, DLEM, ISAM, JSBACH, JULES, LPJ-GUESS, LPJ, LEX-Bern, OCN, ORCHIDEE, ORCHIDEE-MICT, SDGVM, VISIT	Le Quéré et al. (2017)
PM-RS	PM-RS	PM-Gs GPP	2000–2011	daily	1°	LUE and Canopy Conductance	16 EC sites (global)	SDGVM, VISIT GPP is either conductance-limited or radiation limited	Yebra et al. (2015)

(continued on next page)

Table 1 (continued)

Dataset Variable	Model Scheme	Product Name	Temporal cover	Temporal Resolution	Spatial Resolution	Algorithm	Validation	Note	Reference(s)
ET, GPP	LSM	BESS ET, GPP	2000–2015	8-day	1 km, 5 km	BESS, process-based model	113 EC sites (global)	Coupled atmospheric and canopy, radiative transfer processes, with models that computed leaf photosynthesis, stomatal conductance and transpiration on the sunlit and shaded portions of the vegetation and soil	Jiang and Ryu (2016) and Ryu et al. (2011)
	PM-RS	PM-RS ET, EC-LUE GPP	2000–2003	daily	0.5°(lat) × 0.6°(long)	PM-RS, EC-LUE	54 EC sites (AmeriFLUX, EuroFLUX)	Use ET from RS-PM to calculate GPP, Inputs: normalized difference vegetation index (NDVI), photosynthetically active radiation (PAR), air temperature, and the Bowen ratio of sensible to latent heat flux	Yuan et al. (2010)
	PM-RS	BEPS ET, GPP	1982–2016	hourly	0.5°(lat) × 0.6°(long)	BEPS	124 EC sites (global)	ET and GPP from shaded leaves	He et al. (2018)
	PM-RS	PML-V2 ET, GPP	2002–2017	8-day	500 m	PML-V2	95 EC sites (global)	ET and GPP coupled through surface conductance in PM	This study

1 km) ET and/or GPP products available globally (most are > 1 km resolution). Using coarse resolution products (8 km to 0.5 degree (~50 km) resolution) could lead to large uncertainty for plot, catchment and local scale studies. Second, most products do not couple E_t and GPP processes though they are coupled through stomata. For instance, Moderate Resolution Imaging Spectroradiometer (MODIS) products treat these two processes separately, MOD16 ET (Mu et al., 2007; Mu et al., 2011) and MOD17 GPP (Running et al., 2015). Not coupling these two processes can cause the following issues: (i) internal inconsistency between ET and GPP estimates if their forcing data are not same; (ii) inaccurate causality analysis for mean annual values, trends/variation, and water use efficiency. To better understand the influence of carbon-constrained impacts on evapotranspiration, it is critical to credibly couple ET and GPP products at moderate spatial resolution.

Remote Sensing (RS)-based ET models are dominant for regional and global ET estimations in the past few decades (Bastiaanssen et al., 1998a; Bastiaanssen et al., 1998b; Cleugh et al., 2007; Leuning et al., 2008; Long and Singh, 2012; McVicar and Jupp, 2002; Mu et al., 2007; Norman et al., 1995; Ryu et al., 2012; Yang and Shang, 2013; Y.Q. Zhang et al., 2017). All 500 m to 8 km resolution global ET products summarised in Table 1 are driven by RS data since they are spatially and temporally explicit requiring vegetation data, such as vegetation index, leaf area index (LAI) and albedo, and/or temperature and/or soil moisture data.

Among those models, the approaches that combine the Penman-Monteith (PM) equation (Monteith, 1964) with remotely-sensed LAI data have been shown to be biophysically robust (Cleugh et al., 2007; Leuning et al., 2008; Mu et al., 2007; Mu et al., 2011). The PM-based models have been applied to various spatial scales from stand to globe, and to different land cover types (Mallick et al., 2015; Morillas et al., 2013; Mu et al., 2011; Y.Q. Zhang et al., 2017; Zhang et al., 2010; Zhang et al., 2008; Zhang et al., 2016). The main focus of the PM-based modelling framework is the accurate estimate of the surface conductance (G_s), which describes the canopy-soil conductance to water flux. Cleugh et al. (2007) first proposed a simple model for G_s using the MODIS LAI as input.

Leuning et al. (2008) and Zhang et al. (2010) further developed the G_s formulations to account for the physical features of canopy and soil water loss (resulting in the PML (Penman-Monteith-Leuning) ET model). Since then there are two recent notable advances in PML model development. First, Zhang et al. (2016) included evaporation from precipitation intercepted by the vegetation to estimate the three components of ET across globe: E_s , E_t , and E_i (called PML-V1 thereafter). Second, Gan et al. (2018) coupled E_t with GPP using a biophysical canopy conductance (G_c) model (called PML-V2 thereafter) that was successfully tested for 5 Australian ecosystems using 45 site-years (482 months) of flux site data observed at 9 locations. PML-V2 has the following features: (i) coupled estimates of ET and GPP using a relatively simple structure while retaining reasonable biophysical significance; (ii) inclusion of CO_2 concentration change impact on carbon assimilation and canopy conductance; and (iii) easy application to regional and global scales since it only requires readily-available daily meteorological (precipitation, incoming short-wave and long-wave radiation, vapor pressure, air temperature, wind speed, CO_2 concentration) and remote sensing (LAI, albedo and surface emissivity) forcing data.

Google Earth Engine (GEE) is a planetary-scale platform for Earth science data and analysis (Gorelick et al., 2017). It has a multi-petabyte catalog of satellite imagery and geospatial dataset with planetary-scale analysis capabilities that are available for scientists, researchers, and developers to detect changes, map trends, and quantify difference on the Earth's Surface (Gorelick et al., 2017). There are several outstanding regional (Johnson and Iizuka, 2016; Lobell et al., 2015; Midekisa et al., 2017; Patel et al., 2015) and global (Hansen et al., 2013; Pekel et al., 2016) land surface studies performed using GEE, demonstrating its powerful computational infrastructure for parallel computation of geospatial data.

Building on the previous PML studies, this study aims to further improve PML-V2 model structure, develop global parameterisation schemes, and build this model within GEE to estimate coupled ET and GPP, and ecosystem water use efficiency (GPP divided by ET) globally using the climatic (GLDAS) and 500 m resolution MODIS (LAI, albedo, and surface emissivity) data. Novelty of this study include:

- Providing an improved PML-V2 model structure and developing its global parameterisation and validation schemes;
- Coupled estimates of ET and GPP at 500 m and 8-day resolution globally across various plant functional types;
- Comprehensively comparing the PML-V2 estimates to six individual state-of-the-art ET and GPP products;
- Investigating if use of the coupled ET and GPP estimates can strongly improve ecosystem water use efficiency estimates; and
- Exploring spatial pattern and annual variability in ET, GPP and water use efficiency over the past 15 years (2003–2017).

2. PML evapotranspiration models

The PM equation has long been regarded as one of standard methods to estimate E_s and E_t (Cleugh et al., 2007; Leuning et al., 2008; Mu et al., 2007; Mu et al., 2011). PML-V1 (Zhang et al., 2016) uses Leuning surface conductance model together with the PM equation to estimate E_t . Compared to that, PML-V2 uses a water-carbon coupled canopy conductance model to estimate E_t and GPP (Gan et al., 2018). PML-V1 and PML-V2 share the same equations to estimate E_s and E_t . Detailed descriptions of PML-V1 and PML-V2 are provided in Appendix I in the supplementary information.

In this study, PML-V2 is further improved by incorporating the vapor pressure deficit constraint to GPP that is then used to constrain canopy conductance and E_t . In the PML-V2 developed by Gan et al. (2018), GPP are constrained by temperature (Campbell and Norman, 1998; Katul et al., 2010, 2000), but not by vapor pressure deficit (D , in kPa). This study uses D to constrain GPP, and Eqs. (S16) and (S19) (see Supplementary information) are modified using a piecewise function as follows:

$$GPP = f(D)A_{c,g}, \quad (2a)$$

$$f(D) = \begin{cases} 1, & D \leq D_{min}, \\ \frac{D_{max} - D}{D_{max} - D_{min}}, & D_{min} < D < D_{max}, \\ 0, & D \geq D_{max}, \end{cases} \quad (2b)$$

where $A_{c,g}$ is the gross assimilation rate without D constraint, $f(D)$ is the D constraint function adopted from Wang et al. (2014) and Running et al. (2015), D_{min} and D_{max} are parameters (see Table 2).

This version of PML-V2 has eleven free parameters that maintain the physiological significances of the photosynthetic response, namely β , η , m , V_m , D_{min} , D_{max} and vegetation response to environment variables described by D_0 , k_Q , k_A , S_l and F_0 . A summary of these eleven free parameters is provided in Table 2. PML-V2 uses the same fixed parameters (i.e. not sensitive and not calibrated) as PML-V1 to estimate E_s and E_t .

3. Data, parameterisation and model validation

3.1. Climatic and remote sensing forcing data

The 0.25° resolution and 3-hour GLDAS-2.1 meteorological forcings (Rodell and Beaudoin, 2016) from 2002 to 2017, including precipitation, air temperature, vapor pressure, shortwave downward radiation, longwave downward radiation and wind speed, were used to drive the PML-V2 model. Monthly atmospheric CO₂ concentration data were obtained from NOAA globally averaged marine surface monthly mean data (ftp://afpt.cmdl.noaa.gov/products/trends/co2/co2_mm_gl.txt).

To minimize foot print impact of coarse resolution inputs (Zhao et al., 2005), each 0.25° coarse resolution GLDAS-2.1 meteorological input was further interpolated to the 500 m resolution using a widely used approach built in GEE – bilinear interpolation (Ershadi et al., 2013). This minimises the foot print effect, and provides smooth transition for the regions where spatial patterns of GPP and ET are strongly influenced by meteorological inputs (Fig. S1 in Appendix II).

All remote sensing data were obtained from GEE MODIS collection 6 products from 4 July 2002 to 31 December 2017. LAI data were MCD15A3H.006 product (Myneni et al., 2015) which has 500 m spatial resolution and a 4-day temporal resolution. Albedo was obtained from the MCD43A3.006 product (Schaaf and Wang, 2015) with 500 m spatial resolution and a daily temporal resolution. Surface emissivity data, from MOD11A2.006 (Wan et al., 2015), have a 500 m spatial resolution and an 8-day temporal resolution.

To eliminate noise contaminations caused by cloud, shadow, snow, and so on, LAI was smoothed by weighted Whittaker smoother (Eilers, 2003). We used this method for two reasons. First, the Whittaker smoother can deal with the issue of LAI underestimation caused by noise contamination (see Eqs. (3) and (4)). Second, this method performs similarly to the weighted Savitzky-Golay (SG) smoothing filter (Chen et al., 2004), but is much more computationally efficient to be implemented in GEE. Basically, GEE could not handle the weighted SG smoother globally; it still required 1-week to implement Whittaker. In the Whittaker smoother, a weight updating strategy was implemented to capture the upper envelope as shown in Eqs. (3) and (4):

$$\hat{r}_i = \hat{y}_i - y_i, \quad MAD = \text{median}(\text{abs}(\hat{r}_i)), \quad (3)$$

$$w'_i = \begin{cases} (1 - (r_i/6MAD)^2)^2 * w_i, & (0 < r_i < 6MAD) \\ w_i, & (6MAD < r_i \leq 0), \\ 0, & (\text{abs}(r_i) \geq 6MAD) \end{cases} \quad (4)$$

where y_i is the original point, \hat{y}_i is the smoothed point, w_i is point's weight, w'_i is adjusted weight after once smoothing. Initial LAI weights were set using Quality Control flag ('FparExtra_QC') from the MCD15A3H.006 LAI product. Weight for the good-quality points, the points contaminated by aerosol or cirrus, and the points contaminated by snow, cloud or shadow was set as 1, 0.5, and 0.05, respectively.

Compared to LAI, albedo and surface emissivity data were gap-filled using the most efficient approach – linear interpolation from the nearest good-quality points with a eight 8-day window (four 8-day periods before and four 8-day period after; Running et al., 2015). In cases where there were not enough good-quality points available for interpolation, the missing value was first taken as the historical 8-day average and then taken as the historical monthly average if the 8-day average was not available.

Continuous annual land-cover types (2002–2016) were provided by the NASA dataset Center where the Collection 6 of MCD12Q1 based on the International Geosphere-Biosphere Program (IGBP) classification was produced using Friedl's global land-cover algorithms (Friedl et al., 2002; Friedl et al., 2010). The 2016 land-cover type data was used for 2017. Except for land-cover type data, all other MODIS and climatic forcing data were calculated at a 8-day time step (using aggregation and averaging as appropriate) to match with available MODIS products (MOD16A2 for ET and MOD17A2H for GPP). Climatic forcing data were also resampled using the nearest neighbour approach to 500 m spatial resolution to match MODIS data. Detailed flowchart for data processing and PML-V2 modelling is shown in Fig. 1. The quality codes of interpolation information for albedo and emissivity are provided in Table S1 (Appendix III in the supplementary information).

3.2. Flux tower data

There were 95 global flux sites (Fig. 2) from FLUXNET2015 (<http://fluxnet.fluxdata.org/data/fluxnet2015-dataset/>) used to evaluate the PML-V2 model that observed both ET and GPP. These sites cover a wide

Table 2
Summary of ET and GPP parameters used in PML-V2 for each plant functional type. DNF, CSH and CNV share same parameters with ENF, OSH and CRO, respectively. Noting DNF means deciduous needleleaf forest, CSH refers to close shrublands and CNV denotes Cropland/natural vegetation mosaics. These class parameters are used in the global PML-V2 modelling.

Variable	Parameter	Definition	Unit	Parameter value used in this study										
				CaRO	DBF	EBF	ENF	GRA	MF	WSA	OSH	SAV	WET	
ET	D_0	Water vapor pressure deficit of the air	kPa	0.70	0.55	0.54	0.50	0.54	0.50	0.75	0.58	0.81	2.00	
	k_Q	Extinction coefficient of PAR	–	0.10	0.48	0.83	0.91	0.72	0.59	0.75	0.69	1.00	0.64	
	k_A	Extinction coefficient of available energy	–	0.90	0.90	0.90	0.90	0.90	0.68	0.85	0.90	0.90	0.90	
	S_i	Specific canopy rainfall storage capacity per unit leaf area	mm	0.01	0.07	0.10	0.12	0.11	0.13	0.17	0.01	0.05	0.01	
	F_0	Specific ratio of average evaporation rate over average rainfall intensity during storms per unit canopy cover	–	0.16	0.01	0.09	0.06	0.02	0.01	0.11	0.01	0.06	0.01	
GPP	β	Initial slope of the light response curve to assimilation rate (i.e. quantum efficiency)	$\mu\text{mol CO}_2 (\mu\text{mol PAR})^{-1}$	0.03	0.03	0.05	0.04	0.03	0.03	0.04	0.03	0.03	0.03	
	η	Initial slope of the CO_2 response curve to assimilation rate (i.e. carboxylation efficiency)	$\mu\text{mol m}^{-2} \text{s}^{-1} (\mu\text{mol m}^{-2} \text{s}^{-1})^{-1}$	0.07	0.02	0.02	0.07	0.03	0.04	0.03	0.06	0.04	0.04	
	m	Stomatal conductance coefficient	–	8.4	10.9	10.6	8.3	6.3	8.5	6.5	6.3	9.0	25.8	
	V_m	Maximum catalytic capacity of Rubisco per unit leaf area at 25 °C	$\mu\text{mol m}^{-2} \text{s}^{-1}$	20.2	10.8	13.9	13.1	46.4	15.9	13.0	12.8	15.8	16.1	
	D_{min}	The threshold below which there is no vapor pressure constraint	kPa	1.21	0.66	0.66	0.66	0.66	0.66	0.66	1.49	1.03	1.40	
	D_{max}	The threshold above which there is no assimilation	kPa	3.50	6.30	4.57	6.20	3.63	3.50	3.94	4.09	3.70	6.50	

range of global climate regimes from tropical to frigid across 10 plant functional types (PFTs), including: (i) 11 cropland (CRO); (ii) 8 deciduous broadleaf forest (DBF); (iii) 6 evergreen broadleaf forests (EBF); (iv) 22 evergreen needleleaf forests (ENF); (v) 22 grassland (GRA); (vi) 2 mixed forests (MF); (vii) 4 open shrublands (OSH); (viii) 6 savannas (SA); (ix) 8 wetland (WET); and (x) 6 woody savanna (WSA). Site details are presented in Table S2 (Appendix III in the supplementary information). The following criteria are needed to meet for each site, including: (i) mostly homogeneous land cover at 1 km radius from the flux tower (visually determined for each site in GEE); (ii) daily energy balance closure of > 75%; and (iii) > 50 times with 8-day ET and 8-day GPP continuous data available.

3.3. Model calibration

The PML-V2 model was first calibrated and validated by using the flux tower measured meteorological inputs since they have a footprint of 100 m–1 km, making sure the best possible parameter set obtained for each PFT. For global PML-V2 application, the calibrated parameter sets were assigned to each 500 m grid cell according to PFT, and then driven by the bilinear-interpolated GLDAS-2.1 meteorological forcing data together the MODIS data. The PML-V2 ET and GPP obtained from the GLDAS-2.1 forcing data can be fairly compared with other global ET and GPP products, such as the MOD16A2/A3 and MOD17A2 products that adopt the same model calibration and global application strategy (Mu et al., 2011; Running et al., 2015; Ryu et al., 2011).

The PML-V2 model was calibrated using a global optimisation method – the pattern search algorithm – implemented in MATLAB® (The MathWorks, 2018). The pattern search begins at an initial point, then pools mesh points by computing their objective function values until it finds one whose value is smaller than the value at the initial point. So, the pool at one iteration is successful. The algorithm repeats the pooling procedure, based on the point found in last iteration, and it normally converges to the optimum (tolerance of 0.00001 for the change in objective function value) at approximately 50 iterations (Li and Zhang, 2017; Gan et al., 2018).

In the PML-V2 model calibration, each PFT was assigned to one parameter set (i.e. nine parameters) and all flux tower data obtained for each PFT were used to optimise the nine parameters (Table 2). We minimised the following objective function (F) for each PFT:

$$F = 2 - (NSE_{ET} + NSE_{GPP}), \quad (5)$$

where

$$NSE_{ET} = 1 - \frac{\sum_{i=1}^N |ET_{sim,i} - ET_{obs,i}|^2}{\sum_{i=1}^N |ET_{obs,i} - \overline{ET}_{obs}|^2}, \quad (6)$$

$$NSE_{GPP} = 1 - \frac{\sum_{i=1}^N |GPP_{sim,i} - GPP_{obs,i}|^2}{\sum_{i=1}^N |GPP_{obs,i} - \overline{GPP}_{obs}|^2}, \quad (7)$$

where NSE is the Nash-Sutcliffe Efficiency of 8-day ET or 8-day GPP, obs represents 8-day observation, sim represents 8-day simulation, respectively, i is the i th 8-day sample, N is total number of observations for each PFT.

3.4. Model validation and performance metrics

We used leave-one-out cross validation to assess robustness of PML-V2 to predict 8-day ET and 8-day GPP at each flux tower. Each site was left as ‘unmeasured’, and then the data from the remaining same PTF sites were used for model calibration, and finally the optimized parameter set was used for prediction at the ‘unmeasured’. We repeated this procedure across all 10 PFTs in turn isolating each of the 95 flux sites. The predicted GPP/ET values were then compared with the observed ones for cross validation, which explores the transferability of the PML-V2 model from known flux towers to any sites or grid cells.

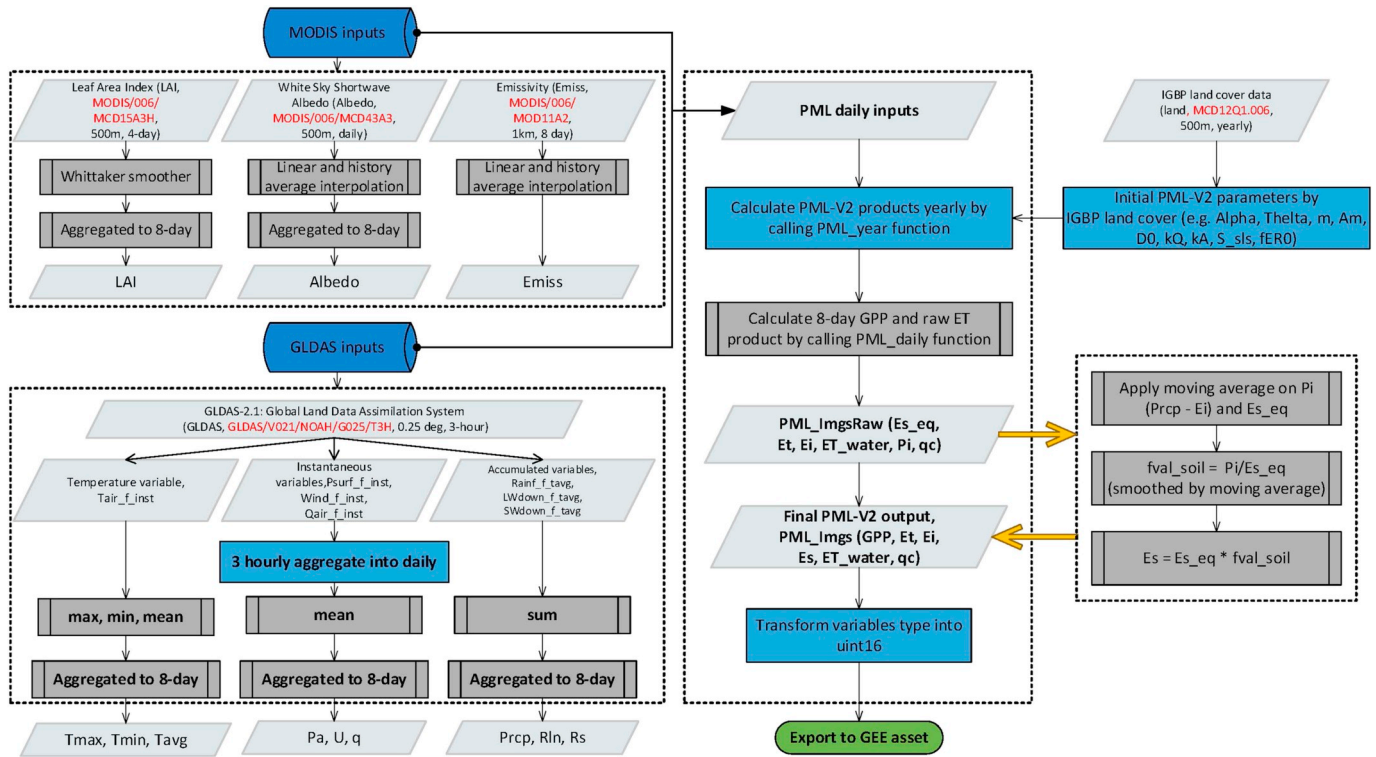


Fig. 1. Flowchart of global forcing data processing and PML-V2 modelling processes. Tmax: daily maximum temperature ($^{\circ}\text{C}$), Tmin: daily minimum temperature ($^{\circ}\text{C}$), Tavg: daily mean temperature ($^{\circ}\text{C}$), Pa: atmosphere pressure (kPa), U: wind speed at 10-m height (m/s), q: specific humidity (kg/kg), Prcp: precipitation (mm/d), Rln: inward longwave solar radiation (W/m^2), Rs: inward shortwave solar radiation (W/m^2), Pi: the difference of Prcp and Ei (mm/d), Es_eq: equilibrium evaporation (mm/d), ET_water: evaporation from water body, snow and ice (mm/d), qc: quality control variable for albedo and surface emissivity.

Both model calibration and cross validation performance for estimating 8-day ET and 8-day GPP were evaluated using four metrics: the calibration metric of *NSE*, and other three including coefficient of

determination (R^2), the Root Mean Square Error (*RMSE*) and Bias (the difference between modelled and observed divided by the observed mean, %).

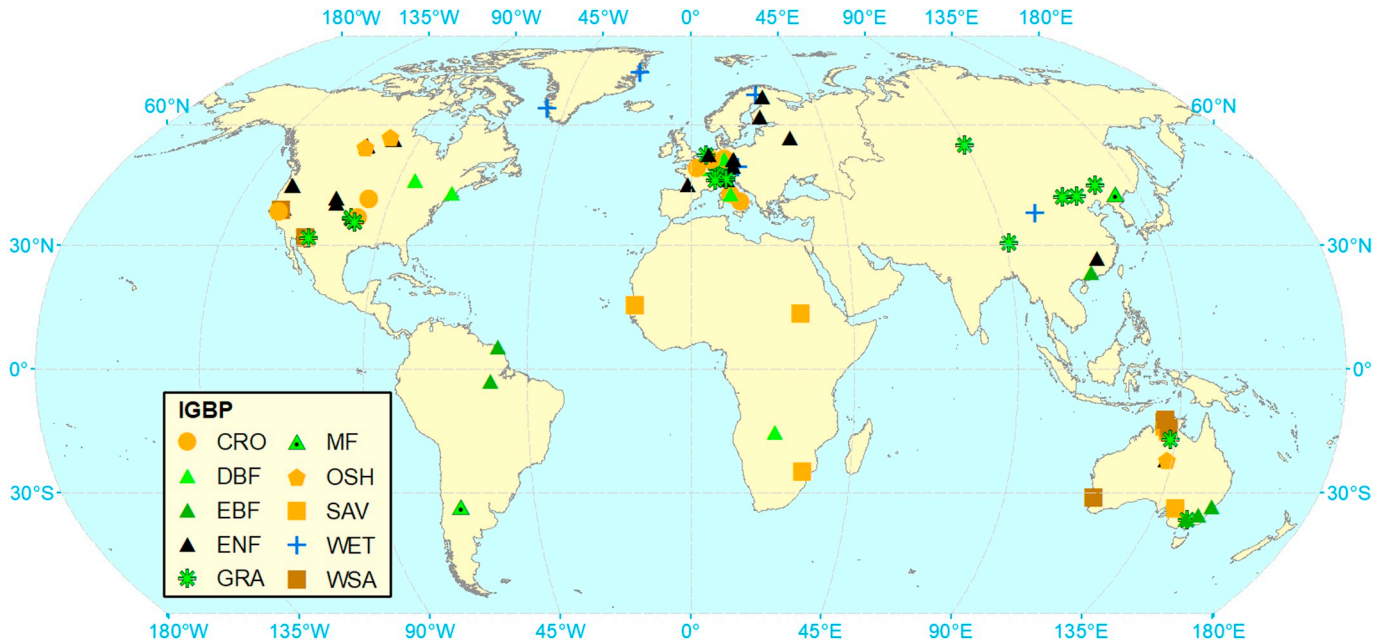


Fig. 2. Location of 95 flux sites used for model calibration and model cross validation. The legend shows the ten major IGBP plant functional types (PFTs) being: cropland (CRO); deciduous broadleaf forest (DBF); evergreen broadleaf forests (EBF); evergreen needleleaf forests (ENF); grassland (GRA); mixed forests (MF); open shrublands (OSH); savannas (SA); wetland (WET); and woody savanna (WSA). An enlarge figure for each site is available from the companion kmz file (Fig 2_st95.kmz).

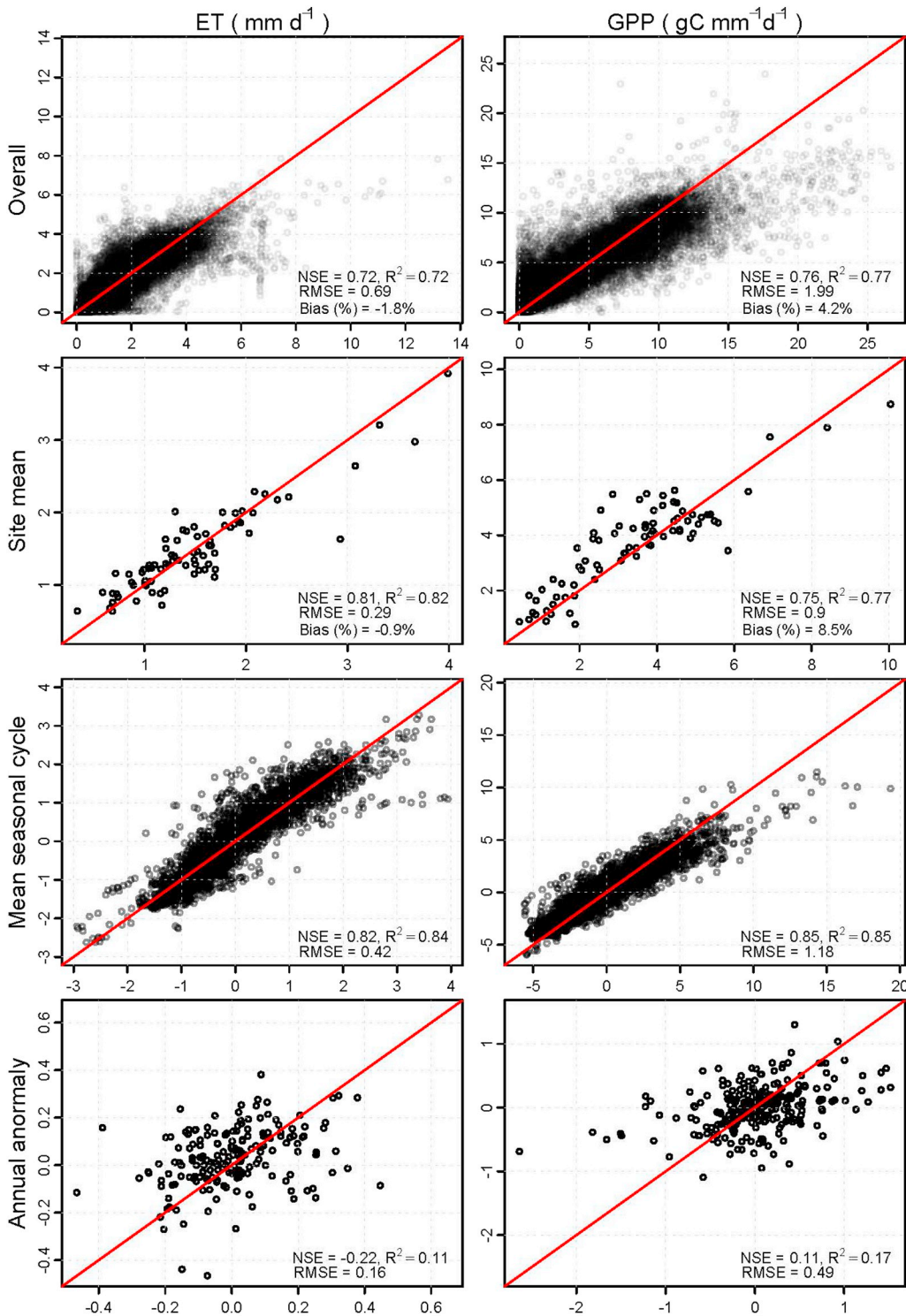


Fig. 3. Scatterplots between observed ET (left column) and GPP (right column) against PML-V2 simulation for 8-day estimates (overall) (top row), site mean (second row), mean seasonal cycle (8-day average across all calendar years) (third row) and annual anomaly (bottom row), obtained from the calibration mode. Mean seasonal cycle of each site is calculated by averaging at least two values obtained from the same 8-day period across different calendar years; site mean is calculated by averaging the mean season cycle across at least 80% of the 46 8-days periods. The 8-day values are averaged into annual if at least 80% of their values are available over the full 15 years; then annual values minus the site mean is the annual anomaly.

4. Results and discussion

4.1. Model calibration versus model validation

Fig. 3 summarises ET and GPP observations and the simulations from the calibrated PML-V2 for all 95 flux sites. Overall, PML-V2 performs well in estimating 8-day ET and GPP, indicated by ET statistical metrics: NSE = 0.72, R^2 = 0.72, RMSE = 0.69 mm d^{-1} , Bias = -1.8%, and GPP statistical metrics: NSE = 0.76, R^2 = 0.77, RMSE = 1.99 $\text{gC m}^{-2} \text{d}^{-1}$, Bias = 4.2%. Similarly, it has good model

performance for site mean and mean seasonal cycle (i.e. 8-day average across all calendar years) for both ET and GPP, with NSE \geq 0.75 and $R^2 \geq$ 0.77. PML-V2 performs least satisfactorily for estimating yearly anomaly, with NSE = -0.22 and RMSE = 0.16 mm d^{-1} for ET and NSE = 0.11 and RMSE = 0.49 $\text{gC m}^{-2} \text{d}^{-1}$ for GPP. This is similar to the finding by Tramontana et al. (2016) who found that machine learning methods perform very satisfactorily for overall, site mean and mean seasonal cycle but least satisfactorily for anomaly.

Compared to the calibration results, the PML-V2 model validation results are only slightly degraded (Fig. 4). For 8-day ET, the calibration

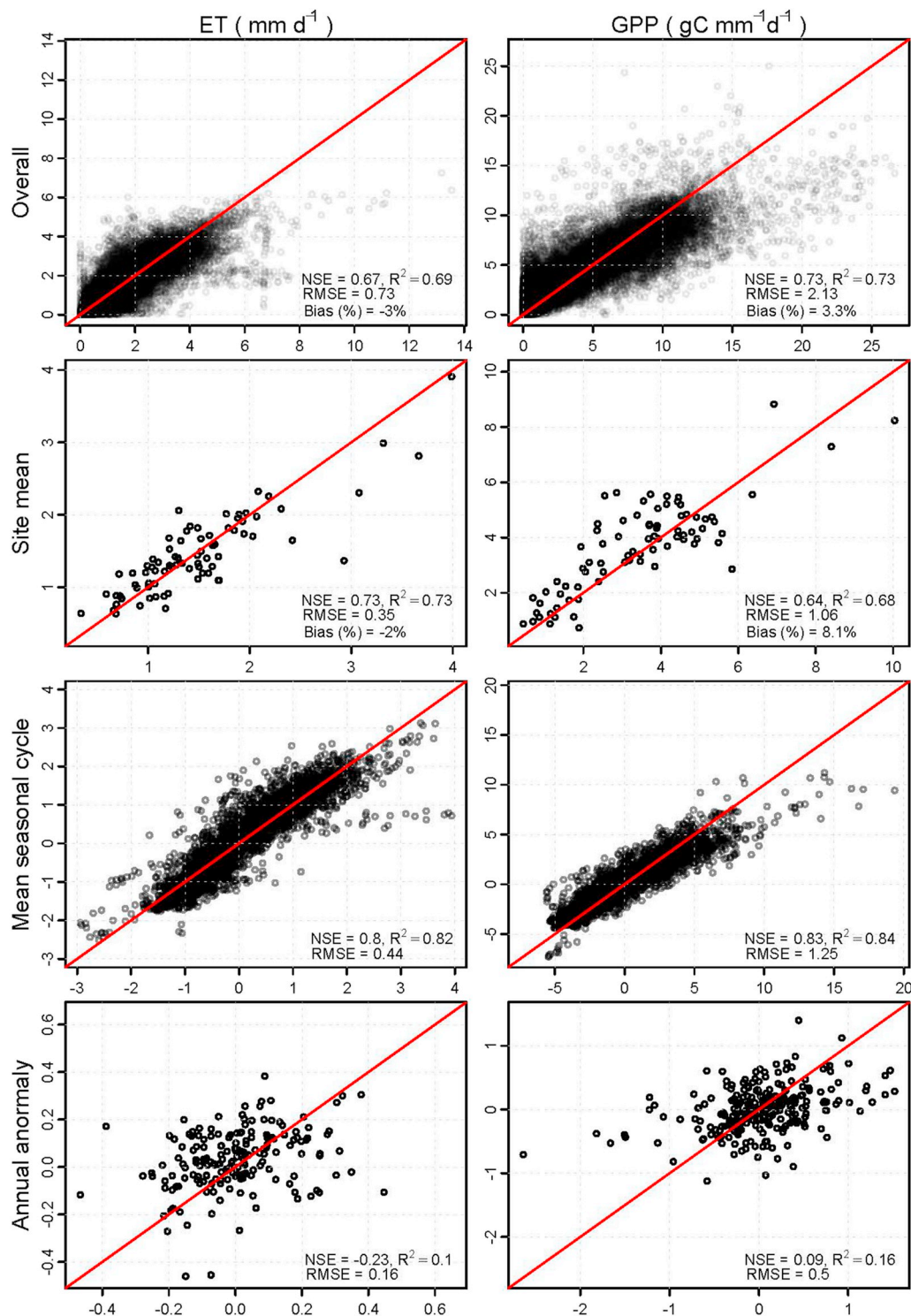


Fig. 4. Same as Fig. 3, but obtained from the cross-validation mode.

NSE is reduced by 0.05 compared to the validation statistics, R² reduced by 0.03, RMSE increased by 0.04 mm d⁻¹, and Bias increased by 1.2%. For 8-day GPP, the calibration NSE and R² are reduced by 0.03–0.04 compared to the validation results, RMSE increased by 0.14 g C m⁻² d⁻¹, Bias even decreased by 0.9%. Similar degradations in ET and GPP are found for site mean, mean seasonal cycle and yearly anomaly. These results indicate the overall robust cross-validation results for both ET and GPP.

Fig. 5 further summarises model performance under calibration and cross-validation modes for each PFT. Model calibrations obtain good

results for all PFTs, indicated by NSE of 8-day ET and R² of ET varying from 0.60 to 0.80, RMSE of ET ranged from 0.45 to 1.20 mm d⁻¹ and Bias varied from -8% to 10%. For 8-day GPP NSE ranged from 0.50 to 0.90, R² varied from 0.50 to 0.90, RMSE ranged from 1.10 to 3.10 g C m⁻² d⁻¹, and Bias varied from -25% to 50%. There are slight degradations from model calibration to model validation. For ET, the NSE degradations are < 0.15 for most PFTs except for OSH where there exists about 0.20 degradation; similar degradations are found for R²; the RMSE degradations (or increases) are < 0.2 mm d⁻¹ for all PFTs; the validation Bias is similar to the calibration Bias for most PFTs except

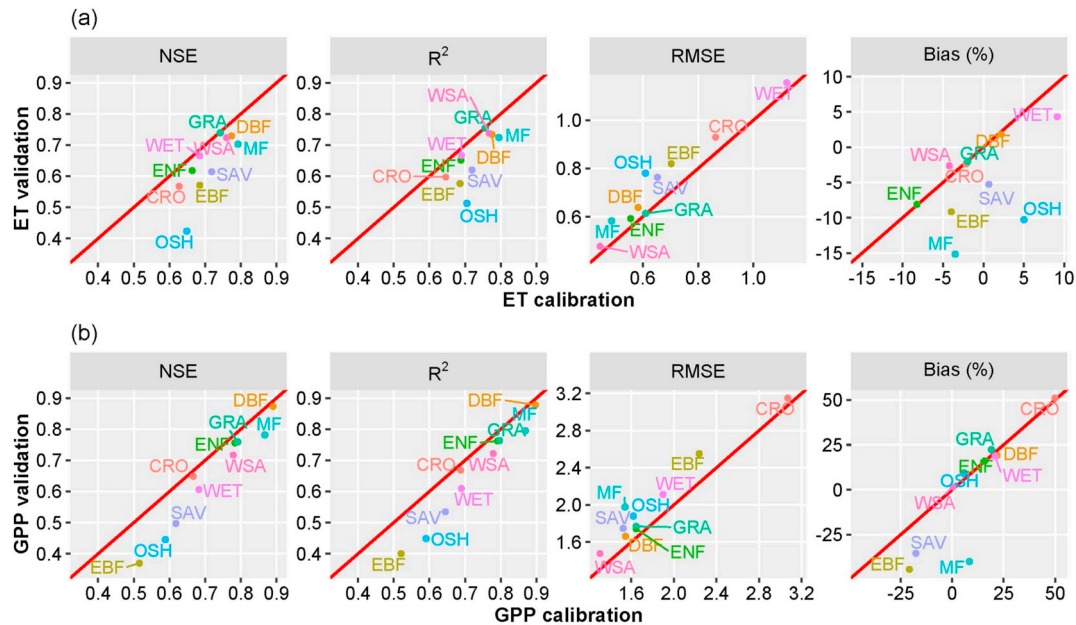


Fig. 5. Comparison between PML-V2 model calibration and its validation across 10 PFTs.

for OSH and MF for both of which the Bias increased by 5–10%. For GPP, the NSE degradations are < 0.10 for most PFTs except for EBF, OSH and SAV where there exists 0.10–0.15 NSE degradation; similar degradation is also found for R^2 ; the RMSE increases are $< 0.3 \text{ g C m}^{-2} \text{ d}^{-1}$ for most PFTs except for EBF and MF of which have the RMSE increased by $\sim 0.4 \text{ g C m}^{-2} \text{ d}^{-1}$; the validation Bias is similar to calibration Bias for most PFTs except for EBF and MF both of which the Bias increased by $\sim 25\%$. Overall, the cross-validation versus calibration comparison demonstrates that PML-V2 is stable and robust across different PFTs.

4.2. Comparing with PML-V1 and MODIS products

Since PML-V1 is widely used for estimating ET for different vegetation types regionally and globally (Anabalon and Sharma, 2017; Cheng et al., 2017; Forzieri et al., 2017; Li et al., 2017; Sun et al., 2017; Wang et al., 2017; Zhang et al., 2017b; Zhang et al., 2016), it can provide a benchmark for evaluating PML-V2. We use the same data set to calibrate PML-V1 (only g_{sx} parameter is optimized) for each PFT. We only present the results obtained from the GLDAS 2.1 meteorological forcing data for both PML-V1 and PML-V2 (Fig. 6(a)). The two versions of PML show similar 8-day ET performance with almost same statistical metrics for majority PFTs. PML-V2 is noticeably better than PML-V1 for OSH and SAV. The overall marginal difference between the two is caused by the similar equations used in the two versions, both of which use the Michaelis-Menten function to define the stomatal response to PAR. Theoretically, the hyperbolic response of stomata to PAR is the dominant control of stomatal conductance under optimum conditions (Kelliher et al., 1995). The advantage PML-V2 is that it maintains the biological energy-driven mechanism and includes CO_2 as an independent environmental constraint (Farquhar et al., 1980; Kelliher et al., 1995; Thornley, 1998; Thornley, 1976). In summary, the coupled PML-V2 model should use dynamic CO_2 concentration to optimal results, not only to maintain its advantage for estimating ecosystem water and carbon fluxes simultaneously, but more importantly, to account for the underlying physical principles governing E_t and GPP rates.

The MODIS ET (Mu et al., 2007; Mu et al., 2011) and GPP (Running et al., 2015) products are widely used for mapping global ET and GPP. Therefore, they can also be used to benchmark PML-V2. To have a fair comparison, we also used the PML-V2 estimates obtained using the

GLDAS 2.1 climate forcing data to compare with MODIS products at the 10 PFTs. Fig. 6(b) compared the PML-V2 ET estimates against MODIS ET estimates (MOD16A2 V6), and Fig. 6(c) compared the PML-V2 GPP estimates against MODIS GPP estimates (MOD17A2H V6) for the 10 PFTs. It is clear that PML-V2 outperforms MOD16A2 for 8-day ET at most PFTs (except for EBF), indicated by NSE and R^2 being 0.05–0.10 higher, RMSE being $0.02\text{--}0.8 \text{ mm d}^{-1}$ lower, and Bias being 0–10% less. For GPP, PML-V2 outperforms MOD17A2H for most PFTs, indicated by NSE and R^2 being 0.05–0.80 higher and RMSE being $0.02\text{--}1.5 \text{ g C m}^{-2} \text{ d}^{-1}$ lower. The MOD17A2H noticeably underestimates 8-day GPP at all PFTs with Bias ranging from -10% to -170% .

4.3. Comparing with other products

Except for the PML-V1 and MODIS products, we also compare other three state-of-the-art ET/GPP products, including GLEAM ET (Miralles et al., 2011a; Miralles et al., 2011b), VPM GPP (Zhang et al., 2017a) and FluxCom GPP (Jung et al., 2017; Tramontana et al., 2016) with estimates from PML-V2 in its cross-validation mode. Table 3 compares model performance among the various ET/GPP methods. It is clear that PML-v2 performs similarly to or noticeably better than other state-of-the-art methods. Table 4 quantifies at how many flux sites PML-V2 outperformed, or underperformed, the other methods for estimating 8-day ET and GPP. We use a threshold of 0.02 for NSE difference suggested by Zhang and Chiew (2009) to differentiate model performance. There are 57, 6 and 30 out of 93 flux sites (GLEAM has no data at 2 flux sites) where PML-V2 performs better than (NSE difference larger than 0.02), similar to (absolute NSE difference < 0.02) and worse (NSE difference less than -0.02) than GLEAM, respectively. There are 50, 8 and 37 out of the 95 flux sites where PML-V2 performs better than, similar to, and worse than VPM, respectively. There are 55, 9 and 31 out of the 95 flux sites where PML-V2 performs better than, similar to, and worse than FluxCom, respectively. Fig. 7 summarises their performance for estimating site mean. For site ET mean, PML-V1 is similar to PML-V2 while MOD16 and GLEAM are poorer than PML-V2. For site GPP mean, VPM is similar to PML-V2 while MOD17 and FluxCom are poorer. In summary, these comparison results (Figs. 6 and 7 and Table 3) provide confidence regarding PML-V2 results for global mapping of ET and GPP.

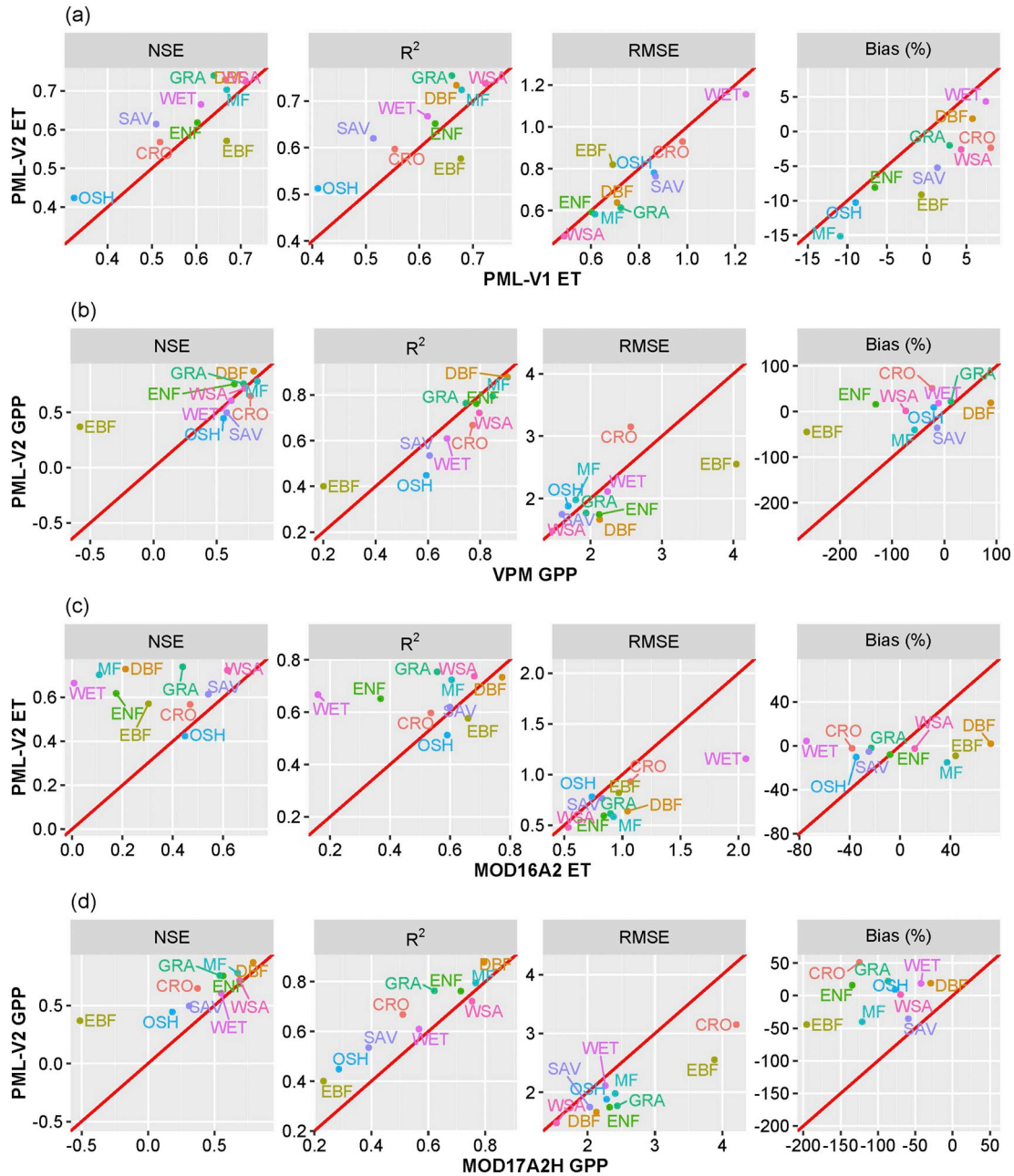


Fig. 6. Comparing PML-V2 (under cross-validation mode) simulations with the simulations obtained from PML-V1 (under cross-validation mode) and MODIS products (MOD16A2 for ET and MOD17A2H for GPP) at each PFT.

Flux site specific tabular performance summaries for the various approaches (i.e., PML-V2, PML-V1, MOD16A2, GLEAM, MOD17A2H, VPM, FluxCom) are provided in Tables S3–S4 (Appendix III in the Supplementary information).

4.4. Water use efficiency

The key feature of PML-V2 is coupled estimation of GPP and ET. Therefore, it can estimate ecosystem water use efficiency (WUE, $\text{g C mm}^{-1} \text{H}_2\text{O}$). This study uses two kinds of WUE: (i) ‘ecosystem WUE’, calculated as GPP divided by ET (at annual or mean annual scale), consistent with Cheng et al. (2017); and (ii) ‘plant WUE’ calculated as GPP divided by E_t at annual or mean annual scale, thereby excluding the ‘inefficient’ water uses caused by E_s and E_i . It is noted that there are many WUE definitions available (McVicar et al., 2002;

Stanhill, 1986; Turner, 1986; Ito and Inatomi, 2012) which are all valid as long as they are explicitly defined, as herein.

Fig. 8 summarises PML-V2 performance when estimating annual WUE for whole ecosystems at the 95 flux sites, in comparison to other model performance (FluxCom GPP/GLEAM ET, VPM GPP/GLEAM ET, and MOD17 GPP/MOD16 ET). PML-V2 performs reasonably well in estimating annual total WUE, indicated by the statistical metrics: NSE = 0.48, $R^2 = 0.49$, RMSE = $0.86 \text{ g C mm}^{-1} \text{H}_2\text{O}$, Bias = 3.3%. Furthermore, PML-V2 is much better than the combinations of other products for estimating ecosystem WUE (Fig. 8). This result indicates the benefit of using the coupled PML-V2 model for estimating ecosystem WUE as the use of the coupled GPP/ET models avoids internal inconsistencies between independent ET and GPP models which provides strong motivation for this research (as stated in our Introduction).

Table 3

Statistical metrics of PML-V2 and other models for estimating ET and GPP, summarised from the 95 flux tower sites. It is noted that Bias is not applicable to mean seasonal cycle and annual anomaly since their mean values approach to zero.

Variable	Model	RMSE	NSE	R ²	Bias (%)	Scale
ET	PML-V2	0.73	0.67	0.69	−3.1	8-day
	PML-V1	0.80	0.62	0.63	1.1	
	MOD16	1.00	0.40	0.49	−8.1	
	GLEAM	0.92	0.50	0.56	−1.4	Site mean
	PML-V2	0.35	0.73	0.73	−2.0	
	PML-V1	0.39	0.65	0.66	1.8	
	MOD16	0.57	0.15	0.42	−6.1	Mean seasonal cycle
	GLEAM	0.59	0.30	0.35	−4.3	
	PML-V2	0.44	0.80	0.82	–	
	PML-V1	0.48	0.76	0.78	–	Annual anomaly
	MOD16	0.62	0.60	0.63	–	
	GLEAM	0.64	0.58	0.65	–	
	PML-V2	0.16	−0.23	0.10	–	Annual anomaly
	PML-V1	0.15	−0.09	0.09	–	
	MOD16	0.14	0.18	0.22	–	
GPP	GLEAM	0.16	−0.06	0.09	–	8-day
	PML-V2	2.13	0.73	0.73	3.3	
	VPM	2.25	0.70	0.71	−10.6	
	MOD17	2.82	0.53	0.59	−26.0	Site mean
	FluxCom	2.83	0.53	0.60	−27.2	
	PML-V2	1.06	0.64	0.68	8.1	
	VPM	1.28	0.49	0.51	−5.7	Mean seasonal cycle
	MOD17	1.30	0.47	0.67	−22.7	
	FluxCom	1.43	0.36	0.57	−23.9	
	PML-V2	1.25	0.83	0.84	–	Annual anomaly
	VPM	1.17	0.85	0.86	–	
	MOD17	1.68	0.69	0.71	–	
	FluxCom	1.71	0.68	0.69	–	Annual anomaly
	PML-V2	0.50	0.09	0.16	–	
	VPM	0.47	0.20	0.21	–	
	MOD17	0.49	0.12	0.13	–	
	FluxCom	0.51	0.06	0.07	–	

Table 4

Site number count for relative performance between PML-V2 and other models. The terms of ‘Better’, ‘Similar’, and ‘Worse’ mean that the 8-day NSE difference between PML-V2 and another model is larger than 0.02, between −0.02 to 0.02, and less than −0.02, respectively.

Model	Variable	PML-V2 compared to others		
		Better	Similar	Worse
PML-V1	ET	64	8	23
MOD16	ET	76	1	18
GLEAM	ET	57	6	30
VPM	GPP	50	8	37
MOD17	GPP	67	5	23
FluxCom	GPP	55	9	31

4.5. Global summary and spatial pattern

We then summarise ET and GPP across the global land surface, excluding water bodies and permanent ice surfaces that are masked by GEE. The 2003–2017 mean ET across the global land surface is $72.8 \times 10^3 \text{ km}^3 \text{ y}^{-1}$ from PML-V2, with the range of previous estimates based on similar study periods (Oki and Kanae, 2006; Trenberth et al., 2007; Zhang et al., 2016). The 2003–2017 mean annual PML-V2 GPP is $145.8 \text{ Pg C y}^{-1}$, which is higher than $\sim 110 \text{ Pg C y}^{-1}$ obtained from the MOD17A2H estimates (Running et al., 2015), $\sim 125 \text{ Pg C y}^{-1}$ obtained from the VPM and FluxCom estimates (Zhang et al., 2017a), but similar to $\sim 140 \text{ Pg C y}^{-1}$ obtained from JULES simulations (Slevin et al., 2017). Welp et al. (2011) suggested that global GPP estimates of $\sim 120 \text{ Pg C y}^{-1}$ are too low, and using the oxygen isotope method they estimated global GPP of $150\text{--}175 \text{ Pg C y}^{-1}$. These results suggest that there is still large uncertainty among the various methods in estimating global GPP.

Fig. 9 summarises spatial distribution of mean annual ET (PML-V2) and mean annual GPP across the globe. ET and GPP exhibit similar spatial patterns. High mean annual ET and GPP are observed in humid tropics, such as South America, central Africa and Southeast Asia. Low mean annual ET and GPP are observed in high latitudes, central Asia, central Australia and western North America.

Fig. 10a and b further summarise spatial patterns of two previously defined WUEs: (i) ecosystem WUE (Fig. 10a); and (ii) plant WUE (Fig. 10b). Ecosystem WUE shows high values in the high-latitude Northern Hemisphere including eastern North America, Europe and central Russia, moderate values in tropics, but low values in arid regions such as central Asia, Sahara, western America and central Australia. Plant WUE shows quite different spatial pattern when compared to the spatial pattern of ecosystem WUE. The most striking differences are the low values of plant WUE occurring in tropical regions, which are less than those from arid regions such as central Australia and western America. This indicates low water use efficiency from tropic forests, such as EBF. This is very interesting since E_t only accounts for $\sim 70\%$ of ET in the tropics (Fig. 10c), while E_t/ET is $< 30\%$ in central Australia and western USA, which indicates that water loss caused by E_i and E_s may control different spatial patterns in GPP/ET and GPP/ E_t .

Fig. 11 shows annual variation of global ET and GPP from 2003 to 2017. Global ET varies between $70 \text{ km}^3 \text{ y}^{-1}$ and $75 \text{ km}^3 \text{ y}^{-1}$ over the past 15 years, with annual linear trends of $0.26 \text{ km}^3 \text{ y}^{-1} \text{ y}^{-1}$ ($p < 0.01$) from PML-V2. The decrease in global ET from 2006 to 2008 is consistent with the previous estimates (Jung et al., 2010; Miralles et al., 2014; Zhang et al., 2016). However, recent strong global ET variability from 2009 to 2017 has not been reported yet. The 2010–2011 peak is largely due to huge rains in arid and semi-arid parts of Australia (Boschat et al., 2015; Fasullo et al., 2013). Global GPP varies between 140 Pg C y^{-1} and 150 Pg C y^{-1} over the past 15 years, which shows a significant increasing trend of $0.20 \text{ Pg C y}^{-1} \text{ y}^{-1}$ ($p < 0.05$), which is almost same as the increased rate found by Cheng et al. (2017) who showed that global GPP is increased by $\sim 15 \text{ Pg C y}^{-1}$ from 2000 to 2011. WUE shows slightly decreased trend ($-0.0044 \text{ g C mm}^{-1} \text{ H}_2\text{O}$) from 2003 to 2017. Nevertheless, it is challenging to comprehensively validate trends in PML-V2 ET and GPP. Sensible hydrological trend analysis normally requires multi-decadal samples (~ 30 or above) (Weatherhead et al., 1998; Jung et al., 2010; Miralles et al., 2014; Zhang et al., 2012; Zhang et al., 2016) while the PML-V2 data only have 15 samples from 2003 to 2017 for each grid and all flux sites have < 12 years of observations on ET and GPP.

4.6. Sources of uncertainty and future directions

Our results indicate that PML-2 performs satisfactorily when evaluated against the flux measurements located across the globe in all major PFTs. However, there are several uncertainties related to the data, parameterisation and algorithm development discussed below. There are two obvious data-related uncertainty sources. First, there are some PFTs with limited flux sites, such as MF with 2 and OSH with 4 (see Fig. 2). This could result in large uncertainty for parameterisation and global mapping. The degradation due to a small sample for ET estimates at these two PFTs are severer than that for the remaining PFTs. Second, uncertainty in land-cover type classification influences parameterisation and accuracy of global GPP and ET mapping. Our study uses the Collection 6 of MCD12Q1 that is more stable than the Collection 5 (Friedl et al., 2010). This is because the supervised classification algorithm is built using more training sites in the Collection 6, making land-cover type more consistent from year-to-year. However, Collection 6 MCD12 suffers spectral confusion between EBF and ENF and there are several classes that are not easily distinguished using coarse resolution data from MODIS (including savannas/grasslands and grasslands/shrublands) (personal communication with Damien Sullia-Menashe, 17 January 2018) which could cause some potential uncertainty in GPP and ET estimates.

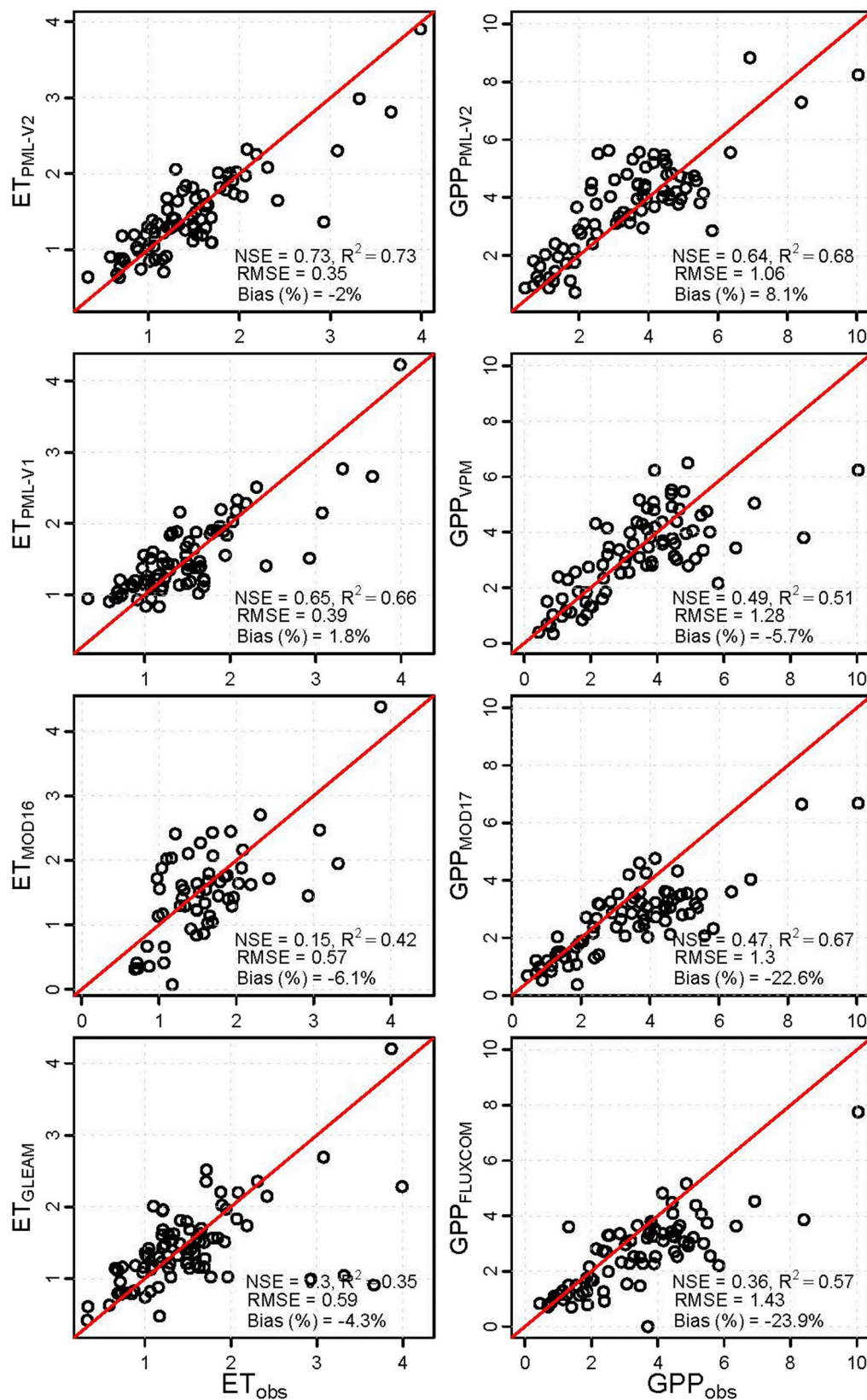


Fig. 7. Scatterplots between the observed ET and simulated for site mean, and between the observed GPP and simulated for site mean at the 95 flux sites.

It is expected that there is uncertainty related to PML-V2 parameterisation. This study selects eleven free model parameters for optimization, as summarised in Table 2. It is possible to include more parameters for better model performance. It is also possible to modify

the current one-leave modelling framework to two-leaf modelling for further improvement (Wang et al., 2014). This, however, will bring more model parameters and hamper its applicability. One of the major objectives of this study is to provide a coupled but parsimonious model

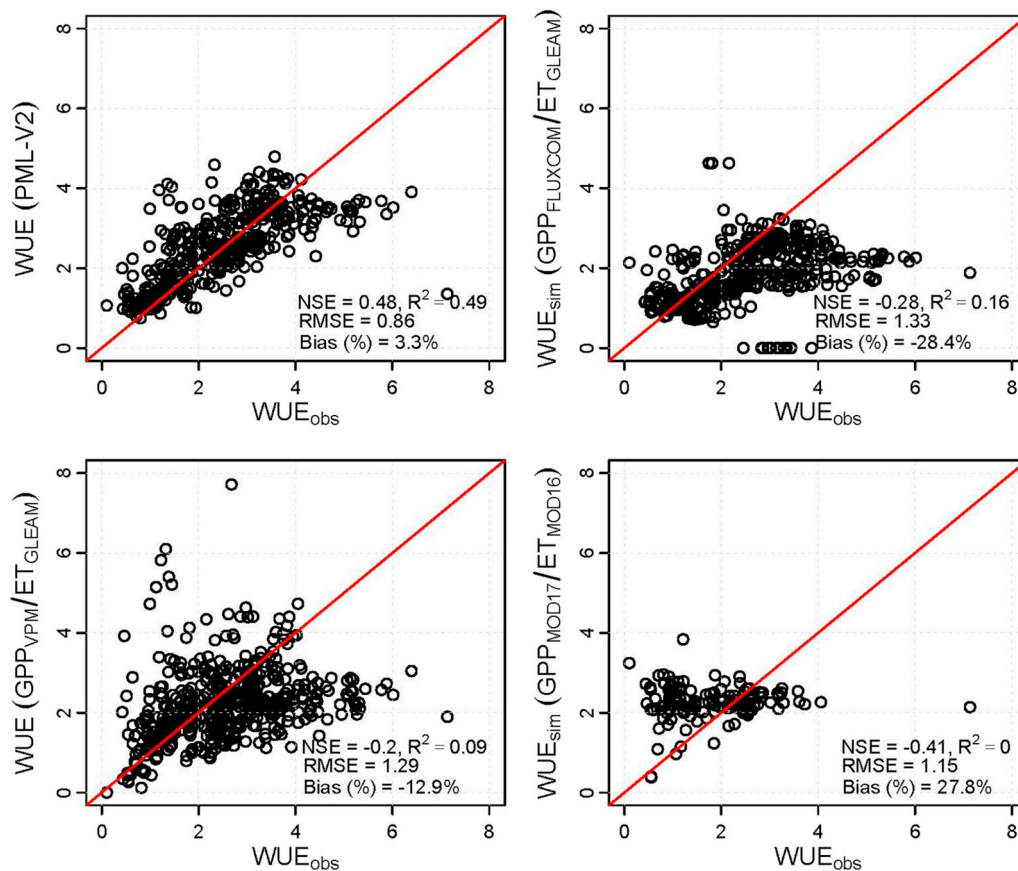


Fig. 8. Scatterplots between the observed annual WUE (GPP/ET, $\text{g C mm}^{-1} \text{H}_2\text{O}$) and simulated at the 95 flux sites.

applied globally, which tries to minimize the parameter equifinality issue (Beven and Freer, 2001). The more the free model parameters are, the more equifinality is. Nevertheless, the parsimonious PML-V2 noticeably outperforms the most individual state-of-the-art ET and GPP products, especially for estimating ecosystem water use efficiency. It demonstrates the usability of the PML-V2, but it is possible to further improve its performance to fit a particular application.

Linear interpolation of albedo and surface emissivity can also contribute to the uncertainty. Fig. 12 shows the global interpolation ratio for albedo and surface emissivity, respectively. It is clear that the interpolation percentage for both is $< 10\%$ in majority of global land surface, indicating overall good quality, and is high in high northern latitudes ($> 60^\circ \text{N}$), southwestern China and small parts of tropics where it is expected low data quality and high uncertainty. It is noted that in the PML-V2 product quality flag interpolation information of both variables is provided.

There is potential for further improving PML-V2 indeed. This study did not consider nutrient stress on GPP and ET constraint, which could lead overestimation of global GPP as discussed in Section 4.5. Further experiments regarding varied LAI and nitrogen impacts on both ET and GPP simulation by PML-V2 can be conducted. Additionally, transpirational cooling needs stomata to open rather than close under increased CO_2 , higher soil moisture availability could contribute to such water loss via transpiration (Cleverly et al., 2016). This dynamic was not considered in the present PML-V2 model and further investigation is required.

It is an open question if it is feasible to use soil moisture to constrain GPP in PML-V2. Currently, PML-V2 does not use soil moisture to constrain GPP. We did try to incorporate flux-site observed soil moisture (up to 50 cm) to constrain GPP, but there are no noticeable improvements for GPP and ET estimates. This suggests that including shallow soil moisture dynamics to constrain GPP has limited benefit to ET estimates. This is particularly the case for our global study as there is no observed dynamic rooting-depth soil moisture dataset available globally. The available microwave dataset only measure soil moisture for top soil layer ($< 5 \text{ cm}$) (Owe et al., 2008), which is much less than the rooting-depth (Yang et al., 2016). Furthermore, some deep-rooted forests show strong resilience from stand to catchment scales (Campos et al., 2013; Smettem et al., 2013; Yang et al., 2016; Yang et al., 2017). They maintain high LAI during drought by accessing deep (i.e., $> 2 \text{ m}$) soil moisture and groundwater (Zhang et al., 2016) and in some extreme cases surface water and groundwater interaction becomes disconnected (Smettem et al., 2013). Therefore, it is challenging to appropriately simulate soil moisture for these ecosystems using traditional global hydrological models. How to optimally include global soil moisture data for improving coupled GPP/ET modelling remains an open question for the carbon and water research communities requiring further research.

It is worth to note that PML-V2 cannot simulate the impact of future increase in atmospheric CO_2 concentration on GPP and ET since it is a diagnostic model, taking LAI as model input to estimate GPP and ET response to atmospheric CO_2 concentration changes. To increase its

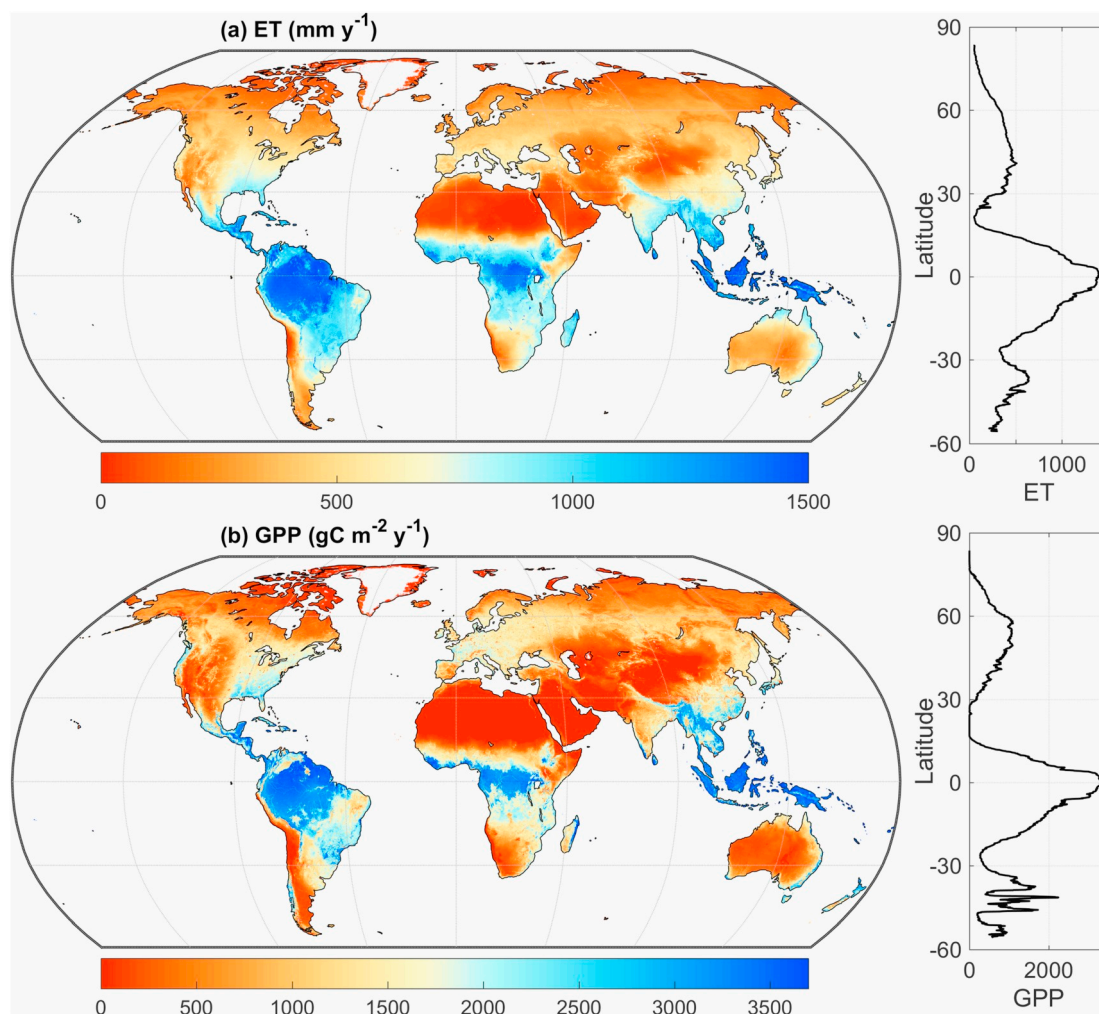


Fig. 9. PML-V2 global average maps of (a) mean annual ET and (b) mean annual GPP for 2003–2017, and their distributions averaged across 1/12° resolution latitudinal bands. These maps are generated at the 1/12° spatial resolution by averaging all 500 m pixels. Water bodies and permanent ice surfaces are excluded for latitudinal averages.

prediction capability, PML-V2 needs to be incorporated with a vegetation growth model to first predict LAI response to CO₂ concentration increase, and then predict the GPP and ET response.

On the other hand, we must re-emphasize PML-V2 advantages as a biophysical process model with solid model performance across various PFTs. Furthermore, considering the parsimonious model structure in PML-V2, it can be easily incorporated into hydrology models to investigate vegetation dynamics and land cover land use change impacts on water and carbon availability at catchment-regional-global scales. Some studies have suggested the remotely sensed evapotranspiration model is very useful for investigating bushfire impacts on streamflow (Poon et al. 2018; Zhou et al., 2013, 2015), and for large-scale runoff predictions (Zhang et al., 2009; Zhang et al., 2008). More efforts should be put on in this area to fully taking the advantage of high-resolution temporally and spatially explicit remote sensing data.

Finally, an objective of this research is to provide 500 m resolution global ET/GPP products for free community use, and to establish the PML modelling framework in GEE. GEE users can access our scripts for applications and potential improvements. PML-V2 can become a

community model. We expect to occasionally update the PML ET/GPP products.

5. Conclusion

This study developed a coupled global evapotranspiration and gross primary production product using a new version of PML-V2 model at 8-day temporal and 500 m spatial resolutions. This product is transparent (freely available scripts and products) and parsimonious (with only nine free model parameters), and based on biophysical process understanding, including the carbon constraint on evapotranspiration, which also provides consistent results using the same forcing data. The product has high accuracy when compared with ground observations from 95 global flux stations located across the globe in all major plant functional types, and outperforms most available evapotranspiration and gross primary production products. Most importantly, PML-V2 largely improves the accuracy of estimating ecosystem WUE, highlighting that using the individual ET and GPP products could lead to large biases for estimating ecosystem WUE at various plant functional

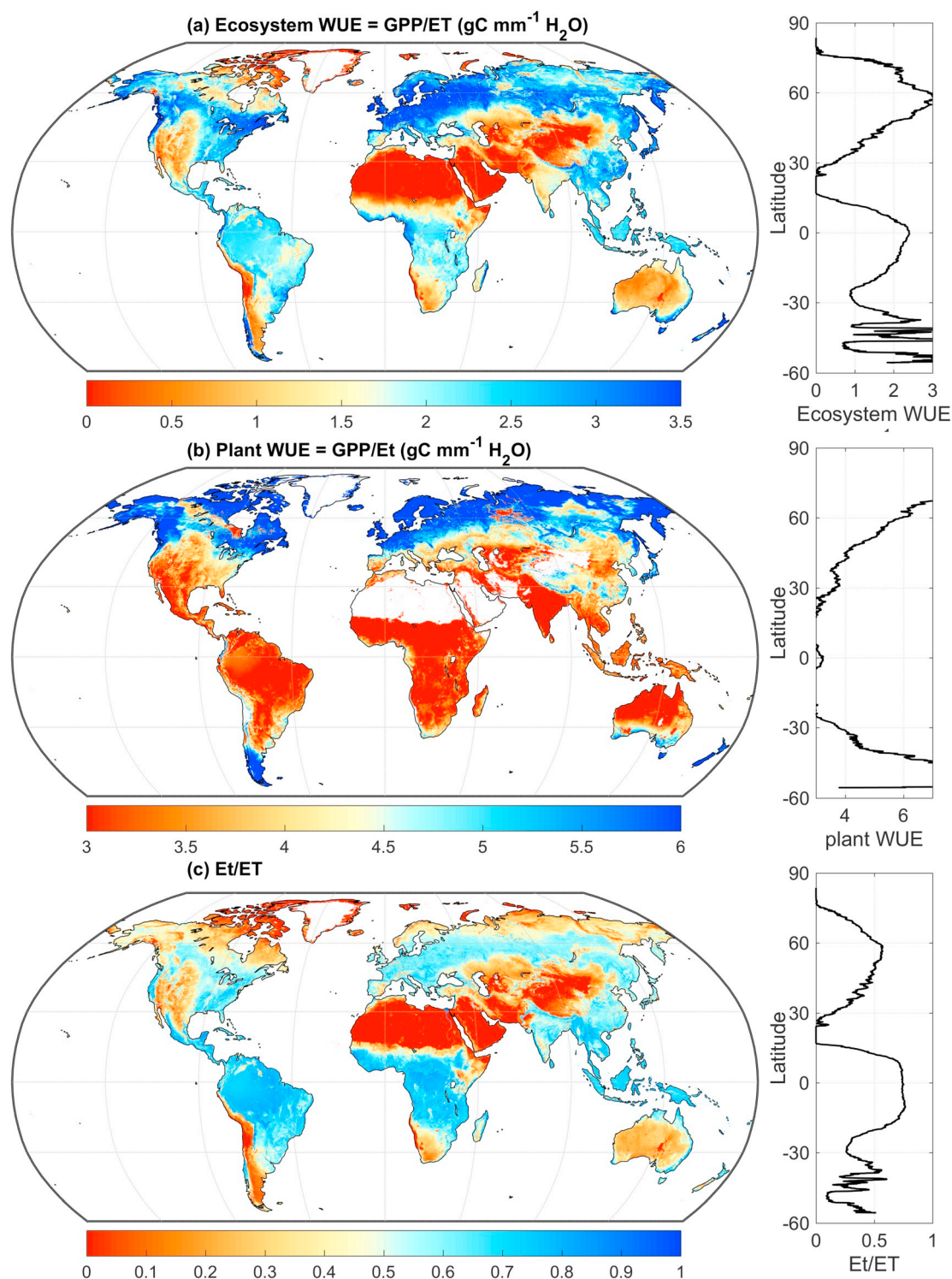


Fig. 10. PML-V2 global average maps of (a) ecosystem WUE, (b) plant WUE, and (c) E_t/ET for 2003–2017, and their distributions averaged across $1/12^\circ$ resolution latitudinal bands. These maps are generated at the $1/12^\circ$ spatial resolution by averaging all 500 m pixels. Water bodies and permanent ice surfaces are excluded for latitudinal averages.

types. Our results indicate that global ET, GPP and ecosystem WUE over the global land surface for the past 15 years (2003–2017) are all significantly ($p < 0.001$) increased, which, in our knowledge, uses the longest MODIS data inputs for understanding global ET, GPP and ecosystem WUE trends.

Our ET/GPP products can be freely used by community for global water and carbon studies through the Google Earth Engine. It can be used together with other similar products for quantifying uncertainty in modelling global evapotranspiration and carbon assimilation. There still exists some room to improve PML-V2 by modifying its model

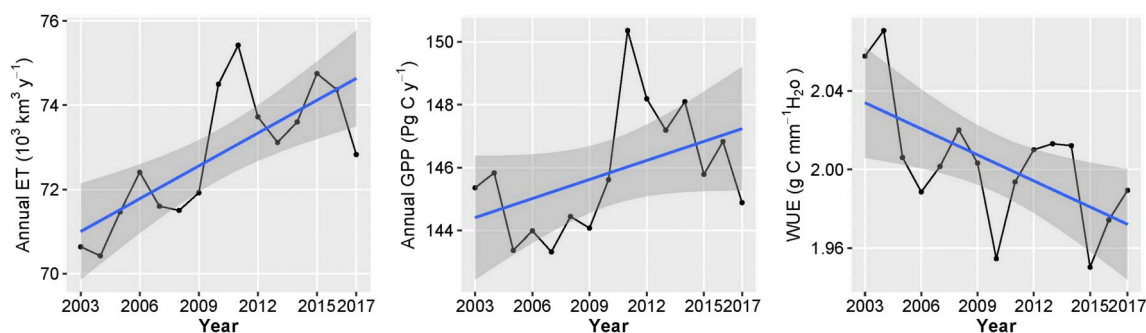


Fig. 11. Annual variation in estimated global ET, GPP and WUE. Part (a) is annual ET with linear trends being $0.241 \times 10 \text{ km}^3 \text{ y}^{-1} \text{ y}^{-1}$ (p value of 1.97×10^{-3}) for PML-V2 and $0.317 \times 10 \text{ km}^3 \text{ y}^{-1} \text{ y}^{-1}$ (p value of 2.60×10^{-4}) from PML-V1. Part (b) is annual GPP with linear trend being $1.248 \text{ Pg C y}^{-1} \text{ y}^{-1}$ (p value of 3.64×10^{-10}), and part (c) is ecosystem WUE with the linear trends being $0.010 \text{ g C mm}^{-1} \text{ H}_2\text{O}$ from PML-V2 and $0.008 \text{ g C mm}^{-1} \text{ H}_2\text{O}$ from PML-V1. In all sub-parts shaded areas show the 95% confidence interval based on the linear regression modelling.

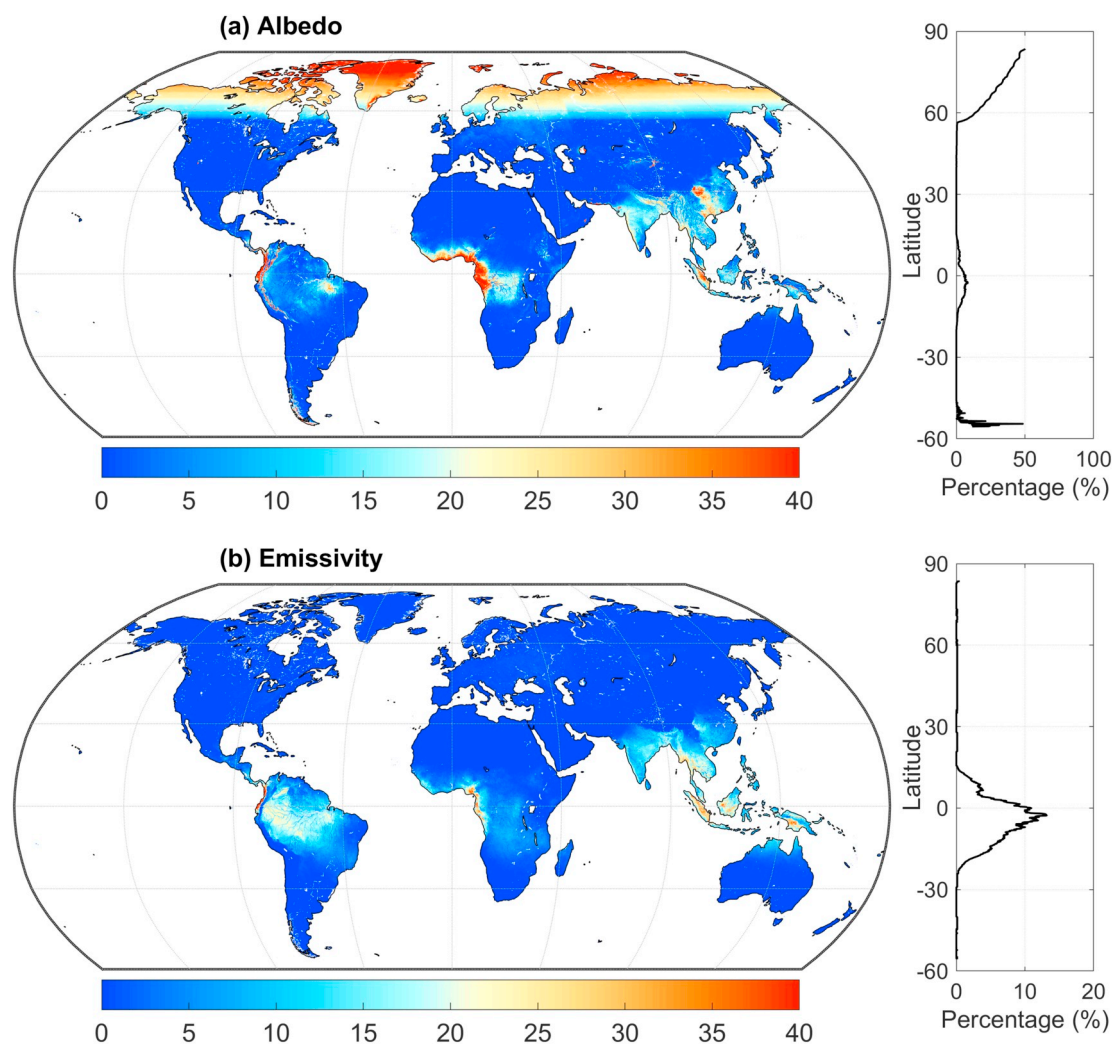


Fig. 12. Global maps of data-gap (or interpolation) percentage for albedo and emissivity.

structure and model parameterisation schemes, and even incorporating multiple forcing inputs for ensemble simulations. This model could also be incorporated into traditional hydrological modelling to investigate hydrological and carbon consequences of land cover change for better catchment water resources management.

Acknowledgements

This study was supported by the CAS Pioneer Hundred Talents

Program, CSIRO International and Sun Yat-Sen University International Program for Ph.D. Candidates. We thank the FLUXNET community for providing flux tower dataset, Yao Zhang for providing VPM GPP data, and the MODIS global land cover team (Mark Friedl and Damien Sulla-Menashe) for providing the Collection 6 of global land cover type dataset. We also like to thank the Google Earth Engine team manager Tyler Erickson for guidance with the model development for product distribution platform. The global ET/GPP products are freely accessed from <https://code.earthengine.google.com/?asset=projects/pml>

evapotranspiration/PML/OUTPUT/PML_V2_8day_v014. The PML-V2 script is freely accessed from <https://github.com/kongdd/PML>. The authors declare no conflict of interest.

Appendix A. Supplementary data

Supplementary data to this article can be found online at doi: <https://doi.org/10.1016/j.rse.2018.12.031>. These data include PML modelling framework, the Google map of the most important areas described in this article.

References

- Anabalon, A., Sharma, A., 2017. On the divergence of potential and actual evapotranspiration trends: an assessment across alternate global datasets. *Earths Future* 5, 905–917.
- Bastiaanssen, W.G.M., Menenti, M., Feddes, R.A., Holtslag, A.A.M., 1998a. A remote sensing surface energy balance algorithm for land (SEBAL). 1. Formulation. *J. Hydrol.* 212–213, 198–212.
- Bastiaanssen, W.G.M., Pelgrum, H., Wang, J., Ma, Y., Moreno, J.F., Roerink, G.J., & van der Wal, T. (1998b). A remote sensing surface energy balance algorithm for land (SEBAL): part 2: validation. *J. Hydrol.* 212–213, 213–229.
- Beer, C., Reichstein, M., Tomelleri, E., Ciais, P., Jung, M., Carvalhais, N., ... Papale, D., 2010. Terrestrial gross carbon dioxide uptake: global distribution and covariation with climate. *Science* 329, 834–838. <https://doi.org/10.1126/science.1184984>.
- Beven, K., Freer, J., 2001. Equifinality, data assimilation, and uncertainty estimation in mechanistic modelling of complex environmental systems using the GLUE methodology. *J. Hydrol.* 249, 11–29.
- Boschat, G., Pezza, A., Simmonds, I., Perkins, S., Cowan, T., Purich, A., 2015. Large scale and sub-regional connections in the lead up to summer heat wave and extreme rainfall events in eastern Australia. *Clim. Dyn.* 44, 1823–1840.
- Campbell, G.S., & Norman, J.M. (1998). *An Introduction to Environmental Biophysics*, 2nd ed. Springer-Verlag, New York.
- Campos, G.E.P., Moran, M.S., Huete, A., Zhang, Y.G., Bresloff, C., Huxman, T.E., Eamus, D., Bosch, D.D., Buda, A.R., Gunter, S.A., Scalley, T.H., Kitchen, S.G., McClaran, M.P., McNab, W.H., Montoya, D.S., Morgan, J.A., Peters, D.P.C., Sadler, E.J., Seyfried, M.S., Starks, P.J., 2013. Ecosystem resilience despite large-scale altered hydroclimatic conditions. *Nature* 494, 349–352.
- Chen, J., Jönsson, P., Tamura, M., Gu, Z., Matsushita, B., Eklundh, L., 2004. A simple method for reconstructing a high-quality NDVI time-series data set based on the Savitzky–Golay filter. *Remote Sens. Environ.* 91, 332–344.
- Chen, M., Rafique, R., Asrar, G.R., Bond-Lamberty, B., Ciais, P., Zhao, F., Reyer, C.P.O., Ostberg, S., Chang, J., Ito, A., Yang, J., Zeng, N., Kalnay, E., West, T., Leng, G., Francois, L., Munhoven, G., Henrot, A., Tian, H., Pan, S., Nishina, K., Viovy, N., Morfopoulos, C., Betts, R., Schaphoff, S., Steinkamp, J., Hickler, T., 2017. Regional contribution to variability and trends of global gross primary productivity. *Environ. Res. Lett.* 12, 105005.
- Cheng, L., Zhang, L., Wang, Y.P., Canadell, J.G., Chiew, F.H.S., Beringer, J., Li, L.H., Miralles, D.G., Piao, S.L., Zhang, Y.Q., 2017. Recent increases in terrestrial carbon uptake at little cost to the water cycle. *Nat. Commun.* 8. <https://doi.org/10.1038/s41467-017-00114-5>.
- Cleugh, H.A., Leuning, R., Mu, Q., Running, S.W., 2007. Regional evaporation estimates from flux tower and MODIS satellite data. *Remote Sens. Environ.* 106, 285–304.
- Cleverly, J., Eamus, D., Luo, Q., Restrepo Coupe, N., Kljun, N., Ma, X., Ewenz, C., Li, L., Yu, Q., Huete, A., 2016. The importance of interacting climate modes on Australia's contribution to global carbon cycle extremes. *Sci. Rep.* 6, 23113.
- Cowan, I., 1982. Regulation of water use in relation to carbon gain in higher plants. In: *Physiological Plant Ecology*. II. Springer, pp. 589–613.
- Dong, B., Dai, A., 2017. The uncertainties and causes of the recent changes in global evapotranspiration from 1982 to 2010. *Clim. Dyn.* 49, 279–296.
- Eilers, P.H.C., 2003. A perfect smoother. *Anal. Chem.* 75, 3631–3636. <https://doi.org/10.1021/ac034173t>.
- Ershadi, A., McCabe, M.F., Evans, J.P., Walker, J.P., 2013. Effects of spatial aggregation on the multi-scale estimation of evapotranspiration. *Remote Sens. Environ.* 131, 51–62.
- Farquhar, G.V., von Caemmerer, S.V., Berry, J., 1980. A biochemical model of photosynthetic CO₂ assimilation in leaves of C₃ species. *Planta* 149, 78–90.
- Fasullo, J.T., Boening, C., Landerer, F.W., Nerem, R.S., 2013. Australia's unique influence on global sea level in 2010–2011. *Geophys. Res. Lett.* 40, 4368–4373.
- Fisher, J.B., Tu, K.P., Baldocchi, D.D., 2008. Global estimates of the land-atmosphere water flux based on monthly AVHRR and ISLSCP-II data, validated at 16 FLUXNET sites. *Remote Sens. Environ.* 112, 901–919.
- Forzieri, G., Alkama, R., Miralles, D.G., Cescatti, A., 2017. Satellites reveal contrasting responses of regional climate to the widespread greening of Earth. *Science* 356, 1140–1144.
- Friedl, M.A., McIver, D.K., Hodges, J.C.F., Zhang, X.Y., Muchoney, D., Strahler, A.H., Woodcock, C.E., Gopal, S., Schneider, A., Cooper, A., Baccini, A., Gao, F., Schaaf, C., 2002. Global land cover mapping from MODIS: algorithms and early results. *Remote Sens. Environ.* 83, 287–302.
- Friedl, M.A., Sulla-Menashe, D., Tan, B., Schneider, A., Ramankutty, N., Sibley, A., Huang, X.M., 2010. MODIS Collection 5 global land cover: algorithm refinements and characterization of new datasets. *Remote Sens. Environ.* 114, 168–182.
- Gan, R., Zhang, Y.Q., Shi, H., Yang, Y.T., Eamus, D., Cheng, L., Chiew, F.H.S., Yu, Q., 2018. Use of satellite leaf area index estimating evapotranspiration and gross assimilation for Australian ecosystems. *Ecohydrology*. <https://doi.org/10.1002/eco.1974>.
- Gorelick, N., Hancher, M., Dixon, M., Ilyushchenko, S., Thau, D., Moore, R., 2017. Google Earth Engine: planetary-scale geospatial analysis for everyone. *Remote Sens. Environ.* 202, 18–27.
- Hansen, M.C., Potapov, P.V., Moore, R., Hancher, M., Turubanova, S.A., Tyukavina, A., Thau, D., Stehman, S.V., Goetz, S.J., Loveland, T.R., Kommareddy, A., Egorov, A., Chini, L., Justice, C.O., Townshend, J.R.G., 2013. High-resolution global maps of 21st-century forest cover change. *Science* 342, 850–853.
- He, L.M., Chen, J.M., Croft, H., Gonsamo, A., Luo, X.Z., Liu, J.N., ... Liu, Y., 2017. Nitrogen availability dampens the positive impacts of CO₂ fertilization on terrestrial ecosystem carbon and water cycles. *Geophys. Res. Lett.* 44 (22), 11590–11600. <https://doi.org/10.1002/2017gl075981>.
- He, L.M., Chen, J.M., Gonsamo, A., Luo, X.Z., Wang, R., Liu, Y., Liu, R.G., 2018. Changes in the shadow: the shifting role of shaded leaves in global carbon and water cycles under climate change. *Geophys. Res. Lett.* <https://doi.org/10.1029/2018GL077560>.
- Ito, A., Inatomi, M., 2012. Water-use efficiency of the terrestrial biosphere: a model analysis focusing on interactions between the global carbon and water cycles. *J. Hydrometeorol.* 13, 681–694. <https://doi.org/10.1175/JHM-D-10-05034.1>.
- Jasechko, S., Sharp, Z.D., Gibson, J.J., Birks, S.J., Yi, Y., Fawcett, P.J., 2013. Terrestrial water fluxes dominated by transpiration. *Nature* 496, 347–350.
- Jiang, C., Ryu, Y., 2016. Multi-scale evaluation of global gross primary productivity and evapotranspiration products derived from Breathing Earth System Simulator (BESS). *Remote Sens. Environ.* 186, 528–547.
- Johnson, B.A., Iizuka, K., 2016. Integrating OpenStreetMap crowdsourced data and Landsat time series imagery for rapid land use/land cover (LULC) mapping: case study of the Laguna de Bay area of the Philippines. *Appl. Geogr.* 67, 140–149.
- Jung, M., Reichstein, M., Bondeau, A., 2009. Towards global empirical upscaling of FLUXNET eddy covariance observations: validation of a model tree ensemble approach using a biosphere model. *Biogeosciences* 6, 2001–2013.
- Jung, M., Reichstein, M., Ciais, P., Seneviratne, S.I., Sheffield, J., Goulden, M.L., Bonan, G., Cescatti, A., Chen, J., de Jeu, R., Dolman, A.J., Eugster, W., Gerten, D., Gianelle, D., Gobron, N., Heinke, J., Kimball, J., Law, B.E., Montagnani, L., Mu, Q., Mueller, B., Oleson, K., Papale, D., Richardson, A.D., Rouspard, O., Running, S., Tomelleri, E., Viovy, N., Weber, U., Williams, C., Wood, E., Zaehle, S., Zhang, K., 2010. Recent decline in the global land evapotranspiration trend due to limited moisture supply. *Nature* 467, 951–954.
- Jung, M., Reichstein, M., Schwalm, C.R., Huntingford, C., Sitch, S., Ahlstrom, A., Arneth, A., Camps-Valls, G., Ciais, P., Friedlingstein, P., Gans, F., Ichii, K., Jain, A.K., Kato, E., Papale, D., Poulter, B., Raduly, B., Rodenbeck, C., Tramontana, G., Viovy, N., Wang, Y.P., Weber, U., Zaehle, S., Zeng, N., 2017. Compensatory water effects link yearly global land CO₂ sink changes to temperature. *Nature* 541, 516–520.
- Katul, G.G., Ellsworth, D.S., Lai, C.T., 2000. Modelling assimilation and intercellular CO₂ from measured conductance: a synthesis of approaches. *Plant Cell Environ.* 23, 1313–1328. <https://doi.org/10.1046/j.1365-3040.2000.00641.x>.
- Katul, G., Manzoni, S., Palmroth, S., Oren, R., 2010. A stomatal optimization theory to describe the effects of atmospheric CO₂ on leaf photosynthesis and transpiration. *Ann. Bot.* 105, 431–442. <https://doi.org/10.1093/aob/mcp292>.
- Keenan, T.F., Hollinger, D.Y., Bohrer, G., Dragoni, D., Munger, J.W., Schmid, H.P., Richardson, A.D., 2013. Increase in forest water-use efficiency as atmospheric carbon dioxide concentrations rise. *Nature* 499 (324–+).
- Kelliher, F.M., Leuning, R., Raupach, M., Schulze, E.-D., 1995. Maximum conductances for evaporation from global vegetation types. *Agric. For. Meteorol.* 73, 1–16.
- Le Quéré, C., Andrew, R.M., Friedlingstein, P., Sitch, S., Pongratz, J., Manning, A.C., ... Zhu, D., 2017. Global carbon budget 2017. *Earth Syst. Sci. Data Discuss.* 2017, 1–79. <https://doi.org/10.5194/essd-2017-123>.
- Leuning, R., Zhang, Y.Q., Rajaud, A., Cleugh, H., Tu, K., 2008. A simple surface conductance model to estimate regional evaporation using MODIS leaf area index and the Penman-Monteith equation. *Water Resour. Res.* 44, W10419.
- Li, H., Zhang, Y.Q., 2017. Regionalising rainfall-runoff modelling for predicting daily runoff: comparing gridded spatial proximity and gridded integrated similarity approaches against their lumped counterparts. *J. Hydrol.* 550, 279–293.
- Li, L.H., Wang, Y.P., Beringer, J., Shi, H., Cleverly, J., Cheng, L., Eamus, D., Huete, A., Hutley, L., Lu, X.J., Piao, S.L., Zhang, L., Zhang, Y.Q., Yu, Q., 2017. Responses of LAI to rainfall explain contrasting sensitivities to carbon uptake between forest and non-forest ecosystems in Australia. *Sci. Rep.* 7. <https://doi.org/10.1038/s41598-017-11063-w>.
- Lobell, D.B., Thau, D., Seifert, C., Engle, E., Little, B., 2015. A scalable satellite-based crop yield mapper. *Remote Sens. Environ.* 164, 324–333.
- Long, D., Singh, V.P., 2012. A two-source trapezoid model for evapotranspiration (TTME) from satellite imagery. *Remote Sens. Environ.* 121, 370–388.
- Mallick, K., Boegh, E., Trebs, I., Alfieri, J.G., Kustas, W.P., Prueger, J.H., Niyogi, D., Das, N., Drewry, D.T., Hoffmann, L., Jarvis, A.J., 2015. Reintroducing radiometric surface temperature into the Penman-Monteith formulation. *Water Resour. Res.* 51, 6214–6243.
- Maxwell, R.M., Condon, L.E., 2016. Connections between groundwater flow and transpiration partitioning. *Science* 353, 377–380.
- McVicar, T.R., Jupp, D.L., 2002. Using covariates to spatially interpolate moisture availability in the Murray–Darling Basin: a novel use of remotely sensed data. *Remote Sens. Environ.* 79, 199–212.
- McVicar, T.R., Zhang, G.L., Bradford, A.S., Wang, H.X., Dawes, W.R., Zhang, L., Li, L.T., 2002. Monitoring regional agricultural water use efficiency for Hebei Province on the North China Plain. *Aust. J. Agric. Res.* 53, 55–76.
- Midekisa, A., Holl, F., Savory, D.J., Andrade-Pacheco, R., Gething, P.W., Bennett, A.,

- Sturrock, H.J.W., 2017. Mapping land cover change over continental Africa using Landsat and Google Earth Engine cloud computing. *PLoS One* 12 (9), e0184926.
- Miralles, D.G., De Jeu, R.A.M., Gash, J.H., Holmes, T.R.H., Dolman, A.J., 2011a. Magnitude and variability of land evaporation and its components at the global scale. *Hydrol. Earth Syst. Sci.* 15, 967–981.
- Miralles, D.G., Holmes, T.R.H., De Jeu, R.A.M., Gash, J.H., Meesters, A.G.C.A., Dolman, A.J., 2011b. Global land-surface evaporation estimated from satellite-based observations. *Hydrol. Earth Syst. Sci.* 15, 453–469.
- Miralles, D.G., den Berg, M.J., Gash, J., Parinussa, R.M., Parinussa, R.M., De Jeu, R.A.M., Parinussa, R.M., Beck, H., Holmes, T., Jimenez, C., Verhoest, N., Dorigo, W., Teuling, A.J., Dolman, A.J., 2014. El Niño-La Niña cycle and recent trends in continental evaporation. *Nat. Clim. Chang.* 4, 122–126.
- Monteith, J., 1964. Evaporation and environment. *Symp. Soc. Exp. Biol.* 19, 205–234.
- Morillas, L., Leuning, R., Villagarcia, L., Garcia, M., Serrano-Ortiz, P., Domingo, F., 2013. Improving evapotranspiration estimates in Mediterranean drylands: the role of soil evaporation. *Water Resour. Res.* 49, 6572–6586.
- Mu, Q., Heinsch, F.A., Zhao, M., Running, S.W., 2007. Development of a global evapotranspiration algorithm based on MODIS and global meteorology data. *Remote Sens. Environ.* 111, 519–536.
- Mu, Q., Zhao, M., Running, S.W., 2011. Improvements to a MODIS global terrestrial evapotranspiration algorithm. *Remote Sens. Environ.* 115, 1781–1800.
- Mueller, B., Seneviratne, S.I., Jimenez, C., Corti, T., Hirschi, M., Balsamo, G., Ciais, P., Dirmeyer, P., Fisher, J.B., Guo, Z., Jung, M., Maignan, F., McCabe, M.F., Reichle, R., Reichstein, M., Rodell, M., Sheffield, J., Teuling, A.J., Wang, K., Wood, E.F., Zhang, Y., 2011. Evaluation of global observations-based evapotranspiration datasets and IPCC AR4 simulations. *Geophys. Res. Lett.* 38, L06402. <https://doi.org/10.1029/2010GL046230>.
- Myneni, R., Knyazikhin, Y., Park, T., 2015. MOD15A2H MODIS/Terra Leaf Area Index/FPAR 8-Day L4 Global 500 m SIN Grid V006. NASA EOSDIS Land Processes DAAC <https://doi.org/10.5067/MODIS/MOD15A2H.006>.
- Norman, J.M., Kustas, W.P., Humes, K.S., 1995. Source approach for estimating soil and vegetation energy fluxes in observations of directional radiometric surface temperature. *Agric. For. Meteorol.* 77, 263–293.
- Oki, T., Kanae, S., 2006. Global hydrological cycles and world water resources. *Science* 313, 1068–1072.
- Owe, M., de Jeu, R., Holmes, T., 2008. Multisensor historical climatology of satellite-derived global land surface moisture. *J. Geophys. Res. Earth Surf.* 113.
- Patel, N.N., Angiuli, E., Gamba, P., Gaughan, A., Lisini, G., Stevens, F.R., Tatem, A.J., Trianni, G., 2015. Multitemporal settlement and population mapping from Landsat using Google Earth Engine. *Int. J. Appl. Earth Obs. Geoinf.* 35, 199–208.
- Pekel, J.F., Cottam, A., Gorelick, N., Belward, A.S., 2016. High-resolution mapping of global surface water and its long-term changes. *Nature* 540, 418–422.
- Raoufi, R., Beighley, E., 2017. Estimating daily global evapotranspiration using Penman–Monteith equation and remotely sensed land surface temperature. *Remote Sens.* 9, 1138.
- Rodell, M., Beaudoin, H., 2016. GLDAS Noah Land Surface Model L4 3 Hourly 0.25 × 0.25 Degree V2.1. Goddard Earth Sciences Data and Information Services Center (GES DISC), Greenbelt, Maryland, USA. <https://doi.org/10.5067/E7TYRXPJKWOQ>. (Accessed 17 Feb 2018).
- Running, S., Mu, Q., Zhao, M., 2015. MOD17A2H MODIS/Terra Gross Primary Productivity 8-Day L4 Global 500 m SIN Grid V006. NASA EOSDIS Land Processes DAAC <https://doi.org/10.5067/MODIS/MOD17A2H.006>.
- Ryu, Y., Baldocchi, D.D., Kobayashi, H., van Ingen, C., Li, J., Black, T.A., Beringer, J., van Gorsel, E., Knohl, A., Law, B.E., Rouspard, O., 2011. Integration of MODIS land and atmosphere products with a coupled-process model to estimate gross primary productivity and evapotranspiration from 1 km to global scales. *Glob. Biogeochem. Cycles* 25, GB4017. <https://doi.org/10.1029/2011GB004053>.
- Ryu, Y., Baldocchi, D.D., Black, T.A., Detto, M., Law, B.E., Leuning, R., Miyata, A., Reichstein, M., Vargas, R., Ammann, C., Beringer, J., Flanagan, L.B., Gu, L., Hutley, L.B., Kim, J., McCaughey, H., Moors, E.J., Rambal, S., Vesala, T., 2012. On the temporal upscaling of evapotranspiration from instantaneous remote sensing measurements to 8-day mean daily-sums. *Agric. For. Meteorol.* 152, 212–222.
- Schaaf, C., Wang, Z., 2015. MCD43A1 MODIS/Terra + Aqua BRDF/Albedo Model Parameters Daily L3 Global - 500 m V006. NASA EOSDIS Land Processes DAAC <https://doi.org/10.5067/MODIS/MCD43A1.006>.
- Schlosser, C.A., Gao, X., 2010. Assessing evapotranspiration estimates from the second global soil wetness project (GSWP-2) simulations. *J. Hydrometeorol.* 11, 880–897.
- Slevin, D., Tett, S.F.B., Exbrayat, J.-F., Bloom, A.A., Williams, M., 2017. Global evaluation of gross primary productivity in the JULES land surface model v3.4.1. *Geosci. Model Dev.* 10, 2651–2670.
- Smettem, K.R.J., Waring, R.H., Callow, J.N., Wilson, M., Mu, Q.Z., 2013. Satellite-derived estimates of forest leaf area index in southwest Western Australia are not tightly coupled to interannual variations in rainfall: implications for groundwater decline in a drying climate. *Glob. Chang. Biol.* 19, 2401–2412.
- Stanhill, G., 1986. Water-use efficiency. *Adv. Agron.* 39, 53–85.
- Sun, S.B., Chen, B.Z., Shao, Q.Q., Chen, J., Liu, J.Y., Zhang, X.J., Zhang, H.F., Lin, X.F., 2017. Modeling evapotranspiration over China's landmass from 1979 to 2012 using multiple land surface models: evaluations and analyses. *J. Hydrometeorol.* 18, 1185–1203.
- The MathWorks, Inc., 2018. Global Optimization Toolbox User's Guide. pp. 11–127.
- Thornley, J.H.M. (1976). *Mathematical Models in Plant Physiology: A Quantitative Approach to Problems in Plant and Crop Physiology*. J. H. M. Thornley. (London; New York: Academic Press).
- Thornley, J., 1998. Dynamic model of leaf photosynthesis with acclimation to light and nitrogen. *Ann. Bot.* 81, 421–430.
- Tramontana, G., Jung, M., Schwalm, C.R., Ichii, K., Camps-Valls, G., Ráduly, B., Reichstein, M., Arain, M.A., Cescatti, A., Kiely, G., Merbold, L., Serrano-Ortiz, P., Sickert, S., Wolf, S., Papale, D., 2016. Predicting carbon dioxide and energy fluxes across global FLUXNET sites with regression algorithms. *Biogeosciences* 13, 4291–4313.
- Trenberth, K.E., Smith, L., Qian, T.T., Dai, A., Fasullo, J., 2007. Estimates of the global water budget and its annual cycle using observational and model data. *J. Hydrometeorol.* 8, 758–769.
- Turner, N.C., 1986. Crop water deficits - a decade of progress. *Adv. Agron.* 39, 1–51.
- Wan, Z., Hook, S., Hulley, G., 2015. MYD11A2 MODIS/Aqua Land Surface Temperature/Emissivity 8-Day L3 Global 1 km SIN Grid V006. NASA EOSDIS Land Processes DAAC <https://doi.org/10.5067/MODIS/MYD11A2.006>.
- Wang, K., Liang, S., 2008. An improved method for estimating global evapotranspiration based on satellite determination of surface net radiation, vegetation index, temperature, and soil moisture. *J. Hydrometeorol.* 9, 712–727.
- Wang, F., Chen, J.M., Gonsamo, A., Zhou, B., Cao, F., Yi, Q., 2014. A two-leaf rectangular hyperbolic model for estimating GPP across vegetation types and climate conditions. *J. Geophys. Res. Biogeosci.* 119, 1385–1398. <https://doi.org/10.1002/2013JG002596>.
- Wang, Y.Y., Zhang, Y.Q., Chiew, F.H.S., McVicar, T.R., Zhang, L., Li, H.X., Qin, G.H., 2017. Contrasting runoff trends between dry and wet parts of eastern Tibetan Plateau. *Sci. Rep.* 7. <https://doi.org/10.1038/s41598-017-15678-x>.
- Weatherhead, E.C., Reinsel, G.C., Tiao, G.C., et al., 1998. Factors affecting the detection of trends: statistical considerations and applications to environmental data. *J. Geophys. Res. Atmos.* 103, 17149–17161.
- Welp, L.R., Keeling, R.F., Meijer, H.A.J., Bollenbacher, A.F., Piper, S.C., Yoshimura, K., Francey, R.J., Allison, C.E., Wahlen, M., 2011. Interannual variability in the oxygen isotopes of atmospheric CO₂ driven by El Niño. *Nature* 477, 579–582.
- Yang, Y., Shang, S., 2013. A hybrid dual-source scheme and trapezoid framework-based evapotranspiration model (HTEM) using satellite images: algorithm and model test. *J. Geophys. Res.-Atmos.* 118, 2284–2300.
- Yang, Y., Donohue, R.J., McVicar, T.R., 2016. Global estimation of effective plant rooting depth: implications for hydrological modeling. *Water Resour. Res.* 52, 8260–8276.
- Yang, Y.T., McVicar, T.R., Donohue, R.J., Zhang, Y.Q., Roderick, M.L., Chiew, F.H.S., Zhang, L., Zhang, J.L., 2017. Lags in hydrologic recovery following an extreme drought: assessing the roles of climate and catchment characteristics. *Water Resour. Res.* 53, 4821–4837.
- Yebara, M., Van Dijk, A.I.J.M., Leuning, R., Guerschman, J.P., 2015. Global vegetation gross primary production estimation using satellite-derived light-use efficiency and canopy conductance. *Remote Sens. Environ.* 163, 206–216.
- Yuan, W., Liu, S., Yu, G., Bonnefond, J.-M., Chen, J., Davis, K., Desai, A.R., Goldstein, A.H., Gianelle, D., Rossi, F., Suyker, A.E., Verma, S.B., 2010. Global estimates of evapotranspiration and gross primary production based on MODIS and global meteorology data. *Remote Sens. Environ.* 114, 1416–1431.
- Zeng, Z., Piao, S., Lin, X., Yin, G., Peng, S., Ciais, P., Myneni, R.B., 2012. Global evapotranspiration over the past three decades: estimation based on the water balance equation combined with empirical models. *Environ. Res. Lett.* 7. <https://doi.org/10.1088/1748-9326/7/1/014026>.
- Zhang, Y.Q., Chiew, F.H.S., 2009. Relative merits of different methods for runoff predictions in ungauged catchments. *Water Resour. Res.* 45, W07412 (doi:10.1029/2008WR007504).
- Zhang, Y.Q., Chiew, F.H.S., Zhang, L., Leuning, R., Cleugh, H.A., 2008. Estimating catchment evaporation and runoff using MODIS leaf area index and the Penman–Monteith equation. *Water Resour. Res.* 44, W10420. <https://doi.org/10.1029/2007WR006562>.
- Zhang, Y., Chiew, F.H.S., Zhang, L., Li, H., 2009. Use of remotely sensed actual evapotranspiration to improve rainfall–runoff modeling in Southeast Australia. *J. Hydrometeorol.* 10, 969–980.
- Zhang, Y.Q., Leuning, R., Hutley, L.B., Beringer, J., McHugh, I., Walker, J.P., 2010. Using long-term water balances to parameterize surface conductances and calculate evaporation at 0.05° spatial resolution. *Water Resour. Res.* 46. <https://doi.org/10.1029/2009WR008716>.
- Zhang, Y.Q., Leuning, R., Chiew, F.H.S., Wang, E.L., Zhang, L., Liu, C.M., Sun, F.B., Peel, M.C., Shen, Y.J., Jung, M., 2012. Decadal trends in evaporation from global energy and water balances. *J. Hydrometeorol.* 13, 379–391.
- Zhang, Y.Q., Pena-Arancibia, J.L., McVicar, T.R., Chiew, F.H., Vaze, J., Liu, C., Lu, X., Zheng, H., Wang, Y., Liu, Y.Y., Miralles, D.G., Pan, M., 2016. Multi-decadal trends in global terrestrial evapotranspiration and its components. *Sci. Rep.* 6, 19124. <https://doi.org/10.1038/srep19124>.
- Zhang, Y., Xiao, X., Wu, X., Zhou, S., Zhang, G., Qin, Y., Dong, J., 2017a. A global moderate resolution dataset of gross primary production of vegetation for 2000–2016. *Earth Syst. Sci. Data* 4, 170165.
- Zhang, Y.Q., Chiew, F.H.S., Pena-Arancibia, J., Sun, F.B., Li, H.X., Leuning, R., 2017b. Global variation of transpiration and soil evaporation and the role of their major climate drivers. *J. Geophys. Res.-Atmos.* 122, 6868–6881.
- Zhao, M.S., Heinsch, F.A., Nemani, R.R., Running, S.W., 2005. Improvements of the MODIS terrestrial gross and net primary production global data set. *Remote Sens. Environ.* 95 (2), 164–176. <https://doi.org/10.1016/j.rse.2004.12.011>.
- Zhou, Y., Zhang, Y., Vaze, J., Lane, P., Xu, S., 2013. Improving runoff estimates using remote sensing vegetation data for bushfire impacted catchments. *Agric. For. Meteorol.* 182, 332–341.
- Zhou, Y., Zhang, Y., Vaze, J., Lane, P., Xu, S., 2015. Impact of bushfire and climate variability on streamflow from forested catchments in southeast Australia. *Hydrol. Sci. J.* 60, 1340–1360.